



Rare earth element input and transport in the near-surface zonal current system of the Tropical Western Pacific

Melanie K Behrens, Katharina Pahnke, Sophie Cravatte, Frédéric Marin, Catherine Jeandel

► To cite this version:

Melanie K Behrens, Katharina Pahnke, Sophie Cravatte, Frédéric Marin, Catherine Jeandel. Rare earth element input and transport in the near-surface zonal current system of the Tropical Western Pacific. *Earth and Planetary Science Letters*, 2020, 549, pp.116496. 10.1016/j.epsl.2020.116496 . hal-03060029

HAL Id: hal-03060029

<https://cnrs.hal.science/hal-03060029>

Submitted on 13 Dec 2020

HAL is a multi-disciplinary open access archive for the deposit and dissemination of scientific research documents, whether they are published or not. The documents may come from teaching and research institutions in France or abroad, or from public or private research centers.

L'archive ouverte pluridisciplinaire **HAL**, est destinée au dépôt et à la diffusion de documents scientifiques de niveau recherche, publiés ou non, émanant des établissements d'enseignement et de recherche français ou étrangers, des laboratoires publics ou privés.

Rare earth element input and transport in the near-surface zonal current system of the Tropical Western Pacific

Melanie K. Behrens^{a*}, Katharina Pahnke^a, Sophie Cravatte^b, Frédéric Marin^b, Catherine Jeandel^b

^aMarine Isotope Geochemistry, Institute for Chemistry and Biology of the Marine Environment (ICBM), University of Oldenburg, Carl-von-Ossietzky-Str. 9-11, 26129 Oldenburg, Germany (*corresponding author: melanie.behrens@uni-oldenburg.de)

^bLEGOS, Université de Toulouse, (IRD, CNES, CNRS, UPS), Toulouse, France

Keywords: Rare earth elements; zonal current system; GEOTRACES

Abstract

Continental sources and current transport play a major role in rare earth element (REE, and other trace element) input and distribution in the Tropical Western Pacific. Here, we present spatially highly resolved distributions of dissolved REE concentrations ([REE]) along three transects in the zonal (extra-)equatorial current system and the Solomon Strait of the Tropical Western Pacific. We use seawater [REE] in combination with direct physical oceanographic observations (e.g., current velocity data) to characterize the geochemical composition, origin and pathways of the complex surface and upper layer currents of the Tropical Western Pacific and to quantify the input fluxes of REEs. We identify Papua New Guinea (PNG) volcanic rocks, sediments, and/or river particles as the key source adding trace elements to the equatorial eastward zonal currents of the Tropical Western Pacific. Our and published data indicate temporal and spatial variability of this input and transport in the PNG source area and the equatorial eastward currents. The westward currents, on the other hand, lack this REE

input signal suggesting lateral transport of preformed seawater [REE]. At the transition between these zonal eastward and westward currents, our data indicate lateral mixing of Eastern and Western Pacific source waters.

1. Introduction

Previous studies from the Tropical Western Pacific pointed out that the supply of micronutrients (e.g., iron, Fe) and other trace elements (e.g., rare earth elements (REE)) in this region likely occurs through fluxes from volcanic island margins such as Papua New Guinea (PNG) and active river input, particularly from the Sepik River (Sholkovitz et al., 1999; Lacan and Jeandel, 2001, 2005; Radic et al., 2011; Slemons et al., 2010, 2012; Grenier et al., 2013, 2014; Labatut et al., 2014; Behrens et al., 2018a; Pham et al., 2019) (Fig. 1a). This was first recognized by Lacan and Jeandel (2001), who suggested that exchange fluxes between PNG margin sediments and adjacent seawater are a source of trace element input to the tropical Pacific zonal current system. Grenier et al. (2013) identified other areas of lithogenic input in the Tropical Western Pacific (e.g., New Ireland, Solomon Islands, Vanuatu, Fiji, Tonga, Samoa) and observed that these fluxes along volcanic island margins can occur throughout the entire water column. In addition, the recent studies of Behrens et al. (2018a, b) and Pham et al. (2019) reported additional areas of seawater REE enrichments near the Philippine Islands in the tropical Northwest Pacific and within the Straits of the Solomon Sea, respectively. Labatut et al. (2014) further suggested net dissolved Fe input through particulate-dissolved exchange processes near PNG that may be of the same nature as those proposed for other particle reactive elements such as REEs, making REEs an ideal tracer for trace element fluxes in our study area.

The relative concentrations of individual dissolved REEs in the ocean are determined by the strength of complexation by carbonate ions that increases from light REEs (LREEs) to heavy

51 REEs (HREEs), resulting in a preferential removal of LREEs over HREEs from seawater
52 (e.g., Byrne and Kim, 1990). Seawater REE patterns are therefore characterized by a typical
53 fractionation pattern with an HREE over LREE enrichment (e.g., Elderfield and Greaves,
54 1982). This characteristic fractionation pattern is visualized by normalization of seawater
55 [REE] to those of a reference water mass or a terrestrial reference standard such as the Post
56 Archean Australian Shale (PAAS) (Taylor and McLennan, 1985). Deviations from this
57 typical REE pattern indicate input ('flat' PAAS-normalized REE pattern) or removal (high
58 PAAS-normalized HREE/LREE ratio) of REEs, or are characteristic of specific sources. In
59 particular, PAAS-normalized positive europium (Eu) anomalies in seawater are characteristic
60 of volcanic input (e.g., Grenier et al., 2013; Molina-Kescher et al., 2018). Enrichments in
61 middle REEs (MREEs) point to river input related to weathering of phosphate minerals (e.g.,
62 Sholkovitz et al., 1999) or release from oxyhydroxides (Haley et al., 2004). REEs are thus
63 ideal to document trace element input, and in combination with direct physical oceanographic
64 observations, to characterize and quantify the geochemical composition, origin and transport
65 of water masses and currents within the ocean. The meridionally and latitudinally high-
66 resolution profiles of dissolved [REE] from the zonal current system of the Tropical Western
67 Pacific and the Solomon Strait presented here (Fig. 1a), provide insight into the small-scale
68 current transport, REE fluxes and lateral advection. In addition, direct combination of the
69 geochemical data with high-resolution physical observations from the same cruise allows the
70 first common detailed assessment of near-surface input and zonal current transport in this
71 region. Based on the combination of elemental concentration data with volume transport data,
72 we estimate element input fluxes and quantify the eastward transport of REE. Additionally,
73 we identify in detail the source areas and origin of the currents based on their distinct
74 Western and Eastern Pacific REE signatures. Moreover, we use published dissolved seawater
75 [REE] and Fe concentration ([Fe]) data from the Tropical Western Pacific (including the

Solomon Sea) (Obata et al., 2008; Slemons et al., 2010, 2012; Grenier et al., 2013; Behrens et al., 2018a; Pham et al., 2019) to evaluate the temporal and spatial variability in this very dynamic area.

2. Study area and hydrography

Our study area lies in the Tropical Western Pacific (Fig. 1a). During the CASSIOPEE cruise with R/V *L'Atalante* (GEOTRACES compliant data GPC05) from July to August 2015, 10 stations were sampled along three transects at 152.5°E, 157.5°E and 165°E within the zonal current system (stations 14, 19, 24, 29, 47, 50, 54, 57, 66, 69) (Fig. 1a). Additionally, two stations were sampled in the eastern and western parts of the Solomon Strait (stations 60 and 63, respectively) (Fig. 1a). Westward and eastward zonal currents were identified during the cruise using acoustic doppler current profiler (ADCP) data (Fig. 1a) (Delpech et al., 2019).

The near surface circulation (≤ 100 m water depth) in the study area is usually dominated east of the Solomon Sea by the westward flowing South Equatorial Current (SEC), weaker at the equator where it can reverse during episodic westerly wind events (Reverdin et al., 1994). In the Solomon Sea, the dominant feature is the surface New Guinea Coastal Current (NGCC) western boundary current that flows along the PNG margin and exits the Solomon Sea through Vitiaz Strait (e.g. Fine et al., 1994; Hristova and Kessler, 2012; Ganachaud et al., 2017). Surface flow is also entering the Solomon Sea through the Solomon Strait (stations 60, 63). The SEC is seasonally weaker during July-August, but the NGCC is stronger (Hristova and Kessler, 2012; Cravatte et al., 2011).

During the CASSIOPEE cruise, the surface circulation was influenced by strong westerly wind events occurring during the onset of El Niño conditions (Oceanic Niño Index, ONI, of +1.5 to +1.8, https://origin.cpc.ncep.noaa.gov/products/analysis_monitoring/ensostuff/ONI_v5.php). These

westerly winds forced eastward surface currents (SC) north of 2°S, which advected surface water from the equatorial western Pacific eastward (Delpech et al., 2019; Fig. 1). During such conditions, surface waters are advected from the coast of PNG to the equator (Radenac et al., 2016). Stations 69, 47, 29 sampled these waters, whereas stations 14, 19, 54, 57, 66 sampled the westward SEC waters (Fig. 1). Stations 24 and 50 sampled the meridionally sheared transition zone between these eastward and the westward currents. In contrast, the sampling campaign during the EUC-Fe cruise (Aug.-Sept. 2006) took place during a weak El Niño event (ONI = +0.5, Slemons et al., 2010, 2012; Grenier et al., 2013).

3. Materials and Methods

3.1. Dissolved REE concentrations

Seawater samples for the analysis of dissolved [REE] were collected at twelve stations. Seawater samples were collected using Niskin bottles and filtered through AcroPak500 filter cartridges (double membrane with 0.8 µm and 0.45 µm pore size) directly from the Niskin bottles or in the onboard laboratory and were acidified to pH = 2 using 6 N HCl (optima quality, Fisher Chemical). At the ICBM of the University of Oldenburg, seawater REEs were purified and pre-concentrated using the automated seaFAST-pico system in offline mode (Elemental Scientific Inc., Nebraska, USA) and measured by isotope dilution (ID) inductively coupled plasma-mass spectrometry (ICP-MS) following the method described in Behrens et al. (2016). In more detail, seawater volumes of ~11-55 mL (pH = 2) per sample were spiked with a multi-element spike containing all REEs (except the mono-isotopic elements) and passed together with a buffer solution (pH = 6) and MilliQ water through the seaFAST column containing a REE-complexing resin (Nobias PA-1) that allows to wash out the seawater matrix. Total procedural onboard blanks of (onboard) MilliQ water and lab blanks

were processed through the seaFAST column and subsequently spiked with a diluted multi-element REE isotope spike for quantification.

Dissolved [REE] were analyzed using a Thermo Finnigan Element 2 ICP-MS coupled to an autosampler (CETAC ASX-100) and a desolvation introduction system (CETAC Aridus 2) (Behrens et al., 2016). Oxide formation rates were 0.01-0.03% (for Ce and Ba) and no corrections for oxide formation were therefore applied. The average instrumental blank of a 2% HNO₃ solution was subtracted for each sample.

Rare earth element ratios and anomalies presented in this study are based on PAAS-normalized (Taylor and McLennan, 1985) REE data (PAAS-normalization indicated by subscript N in the following). The Eu anomaly is calculated as $[Eu/Eu^*]_N = [3 \times Eu_N / (2 \times Sm_N + Tb_N)]$ (Zhang et al., 2008).

The accuracy was checked with replicates of the GEOTRACES seawater standard SAFe 3000 m and average [REE] agreed within the 2 SD confidence interval of the published intercomparison study (Behrens et al., 2016) (Table S1a). Note that the REE data of Grenier et al. (2013) and Pham et al. (2019), both carried out at LEGOS (Toulouse) and used for comparison in this study (see section 5.2.), are consistent with our data, as this laboratory successfully participated in the intercomparison study of Behrens et al. (2016). The external standard deviation is derived from independently processed seawater replicates from a sample from station 50 at 1001 m water depth (sample 50-2-8, n = 4) (Table S1b). If the internal standard deviation of a sample was higher than this external value, the internal value is reported. Average total procedural onboard (n = 8) and lab blanks (n = 14) were $\leq 1.9\%$ for all REEs, except for Ce (4.9%, n = 20, and 28%, n = 2) of the average sample concentration. The standard deviation for $(Yb/Er)_N$ and $(Eu/Eu^*)_N$ are ± 0.03 and ± 0.02 (1 SD), respectively, and are based on sample replicates (sample 50-2-8, n = 4).

3.2. Near-surface currents

During the CASSIOPEE cruise, horizontal currents were recorded along the ship track with two Shipboard-ADCPs (S-ADCP) OS-38 kHz and OS-150 kHz. S-ADCP data were processed and calibrated using the CODAS software. The OS-150 kHz provides zonal and meridional currents with a typical 8-m depth resolution (Delpech et al., 2019), the first bin being at 20 m depth. The transports in the surface layer are computed assuming a negligible vertical shear above 20 m and assigning the value of the shallowest observed velocity to all depths above that observation. To estimate the temporal variability of the transports in the Solomon Sea straits, data from moorings deployed in the straits during July 2012-March 2014 are used (Alberty et al., 2019).

In addition, the large-scale currents context at the time of CASSIOPEE cruise is deduced from the OSCAR surface current product (Bonjean and Lagerloef, 2002). These near-surface currents are representative of the 0-30 m layer, and are directly estimated from sea surface height, near surface vector wind and sea surface temperature data. They are produced on a $1/3^\circ$ grid, 5 days temporal resolution, and are analyzed for the CASSIOPEE period in July-August 2015.

4. Results

Dissolved seawater [REE] (Table 1), REE ratios and anomalies, as well as hydrographic characteristics (including currents) (Table S2) are available on Pangaea (www.pangaea.de) under <https://doi.org/10.1594/PANGAEA.913672>. In order to present all our surface REE data and allow inclusion of and comparison with published data, we defined a surface (0-35 m water depth) and near-surface (40-100 m water depth) layer. All our samples show positive PAAS-normalized Eu anomalies of 1.13-1.27, with higher values found in the equatorial zonal eastward SC compared to the westward SEC in the open ocean transect at 165°E (Fig.

2a-c; Table S2). In addition, the near surface water is marked by a depletion in HREEs from erbium (Er) to lutetium (Lu) in PAAS-normalized REE patterns (Fig. S1) at all our stations, this depletion being less pronounced in the equatorial zonal eastward SC (stations 69, 47, 29) than in the westward SEC (stations 14, 19, 54, 57, 66) (Fig. S1a-c). This depletion is illustrated using the normalized Yb/Er ratio. In addition, we observe a small natural positive Gd anomaly in all our seawater samples that typically occurs in PAAS-normalized REE patterns (Fig. S1) due to the higher stability of Gd carbonate complexes relative to its neighbors (e.g., de Baar et al., 2018).

4.1. Surface water [REE] in the study area (0-35 m water depth)

Highest surface water [REE] (e.g., Nd = 6.0-8.1 pmol/kg) of all stations of this study are observed within the equatorial zonal eastward SC (stations 69, 47, 29) (Figs. 3a, c; S1a, b). In the extra-equatorial westward SEC, on the other hand, we find lowest surface water [REE] of all our stations (Nd = 3.2-3.6 pmol/kg, stations 14, 19, 54, 57, 66, Fig. 3a, c), with a marked depletion of the HREEs expressed by low $(Yb/Er)_N$ ratios of 0.55-0.65 compared to those of the SC ($(Yb/Er)_N = 0.79-0.84$) (Figs. 3b; S1a, b).

Surface water sampled at the transition of the SEC and SC (stations 24 and 50) that flows into the Solomon Sea via the Solomon Strait (stations 60 and 63) shows slightly higher [REE] than within the SEC (Nd = 4.1 ± 0.3 pmol/kg, n = 7) (Figs. 3a, c; S1a, b).

4.2. Near-surface water [REE] in the study area (40-100 m water depth)

In the equatorial zonal eastward SC, near-surface water [REE] ($[Nd] = 4.0-4.7$ pmol/kg) are slightly enriched relative to those of the extra-equatorial zonal westward SEC ($[Nd] = 3.3-3.7$ pmol/kg), and decrease vertically from the surface to 100 m by up to 50% for [Nd] at station 69 (Figs. 3 c, d; S1b, c). Near-surface water [REE] within the SEC, on the other hand, are

similar to those of the overlying surface water ($\text{Nd} = 3.2\text{-}3.6 \text{ pmol/kg}$) (Figs. 3 c, d; S1b, c). In the Solomon Strait near New Britain, surface to near-surface water [REE] increase by $\sim 2.3 \text{ pmol/kg Nd}$ (station 63) (Figs. 3a, c, d; S1a-c). In the following, we will compare our new REE data with published data in the study area (Grenier et al., 2013; Pham et al., 2019; Behrens et al., 2018a). All the data considered here lie within the surface mixed layer. However, the stations were sampled during different seasons and years (EUC-Fe cruise, Aug.-Sept. 2006; PANDORA cruise, July-Aug. 2012; SO223T cruise, Sept.-Oct. 2012), and thus reflect the hydrographic and geochemical data at the particular time of sampling in this very dynamic area.

5. Discussion

5.1. Rare earth element fluxes in the tropical West Pacific source area and surface and near-surface zonal current system

5.1.1. Surface water (0-35 m water depth)

Surface water normalization of [Nd] and [REE] to those of upstream station GeoB17019 (Behrens et al., 2018a, black inverted triangle in Fig. 4a, b; normalized [Nd] referred to as Nd_{norm}) indicates a more than 2-fold enrichment of REEs in the eastward SC (Fig. 5a, b). In addition, we observe elevated positive $(\text{Eu}/\text{Eu}^*)_{\text{N}}$ of surface water at the open ocean transect 165°E ($(\text{Eu}/\text{Eu}^*)_{\text{N}} = 1.23$ and 1.26 ± 0.02 , station 29, Fig. 2a, b) and at nearby stations GeoB17015 to -17 ($(\text{Eu}/\text{Eu}^*)_{\text{N}}$ up to 1.25, Behrens et al., 2018a) compared to stations 14 and 19 in the westward SEC ($(\text{Eu}/\text{Eu}^*)_{\text{N}} = 1.16\text{-}1.18 \pm 0.02$, Fig. 2a, b). This indicates trace element input from PNG, with an imprint of the positive $(\text{Eu}/\text{Eu}^*)_{\text{N}}$ signal from PNG volcanic source rocks (e.g. $(\text{Eu}/\text{Eu}^*)_{\text{N}} \sim 1.4\text{-}1.5$, Woodhead et al., 2010) onto seawater, and

225 eastward transport to the equator via the western boundary current (NGCC) feeding the
 226 equatorial eastward SC.

227 The combination of physical data with [REE] allows the quantification of trace element input
 228 ($F_{\text{input}} = W \times [\text{Nd}]$, with W as mass transport (Sv) and $[\text{Nd}]$ as dissolved Nd concentration
 229 (pmol/kg)). In Vitiaz Strait, the mass transport in the 0-35 m layer varies from -0.37 Sv to 1.1
 230 Sv in 2012-2014 (Alberty et al., 2019), depending on the season (stronger during June-
 231 August, weaker during February-April, possibly reversing direction) and the El Niño
 232 Southern Ocean Oscillation (ENSO) phase (stronger during El Niño, weaker during La Nina).
 233 This transport was is in the upper range during the PANDORA cruise in July-Aug. 2012
 234 (1.05 Sv, based on SADCP data), and during the CASSIOPEE cruise in July-Aug. 2015,
 235 which took place at the onset of the strongest El Niño event of the early 21st century
 236 (Delpech et al., 2019). We estimate the surface water Nd flux in the Vitiaz Strait to be F_{Vitiaz}
 237 $= 22.3 \text{ t(Nd)/yr}$ during PANDORA and CASSIOPEE (using water transport of 1 Sv at 0-35 m
 238 water depth at station 77 with $[\text{Nd}] = 4.9 \text{ pmol/kg}$, Pham et al., 2019). The Vitiaz Strait
 239 (station 77, Fig. 1a) is located upstream of PNG and the Sepik River.

240 For the Sepik River, we determine dissolved Nd input fluxes of 0.39 t(Nd)/yr and 0.77
 241 t(Nd)/yr using minimum discharge in Aug./Sept. ($2500 \text{ m}^3/\text{s}$) and maximum discharge in
 242 March/April ($5000 \text{ m}^3/\text{s}$), respectively (Fig. 12a of Delcroix et al., 2014 and references
 243 therein) and dissolved $[\text{Nd}]$ of 34 pmol/kg at a salinity of 10 (Sholkovitz et al., 1999) and
 244 assuming 86% removal of dissolved Nd in the estuary. Sepik River water $[\text{Nd}]$ was sampled
 245 in Aug. 1997 during the peak season of the SW monsoon period (June-Nov.) (Sholkovitz et
 246 al., 1999), when surface water is transported from PNG to the equator (Lindstrom et al.,
 247 1987), and hence the imprint of an island weathering signature to equatorial surface water
 248 was suggested (e.g., Milliman, 1995; Sholkovitz et al., 1999). Our estimated dissolved Sepik
 249 River input fluxes of 0.39 t(Nd)/yr and 0.77 t(Nd)/yr are respectively 1.7% and 3.5% of the

250 estimated surface water Nd flux of 22.3 t(Nd)/yr from the Vitiaz Strait, calculated above.
 251 That is, the river input flux could account for a 0.1-0.2 pmol/kg enrichment in Nd or 3% and
 252 6% of the observed seawater REE enrichment of 3.2 pmol/kg Nd found in the equatorial
 253 eastward SC downstream of the Sepik River at station 69. This implies a missing flux of
 254 12.0-12.6 t(Nd)/yr. In the following, we address the potential uncertainties of these estimates
 255 (e.g., Sepik River discharge, Nd removal in the estuary, sampling location, temporal
 256 variability in Nd distribution and water transport data).
 257 Sholkovitz et al. (1999) mentioned that river water discharge data from PNG (i.e. the Sepik
 258 River) was poorly documented, and at that time, they had to assume that half of the amount
 259 of water that is discharged from all PNG rivers is discharged to the northern coast of PNG.
 260 Thus, they used a total northern PNG river flow estimate that is 10-fold higher than we used
 261 in this study. In addition, Sholkovitz et al. (1999) assumed only 50% of removal of dissolved
 262 Nd for the total northern PNG estuaries. In contrast, for the Sepik River estuary, we used
 263 86% of Nd removal based on dissolved Sepik River water Nd data in the estuary reported in
 264 Table 2 of Sholkovitz et al. (1999), who also mentioned that this removal rate is typical of
 265 estuaries world wide (e.g., Goldstein and Jacobsen, 1988) and consistent with more recent
 266 estimates of $71 \pm 16\%$ (Rousseau et al., 2015). However, even if we consider the uncertainty
 267 of 16%, as suggested by Rousseau et al. (2015) for this estuarine removal, the river input flux
 268 could account for a 0.2-0.3 pmol/kg enrichment in Nd or 6% and 9% of the observed
 269 seawater REE enrichment of 3.2 pmol/kg Nd.
 270 Other potential uncertainties of our estimation may be the sampling location and the temporal
 271 variability in Nd distribution and water transport data. We therefore compare the dissolved
 272 surface water [Nd] of 4.9 pmol/kg at station 77 (Vitiaz Strait, PANDORA, July 2012, Pham
 273 et al., 2019) and equatorial surface water [Nd] (up to 8.1 pmol/kg) at our station 69
 274 (CASSIOPEE, Aug. 2015) to that of the equatorial nearby station GeoB17016 ([Nd] = 6.2

275 pmol/kg, Sept. 2012, Behrens et al., 2018a). This station was sampled 1-2 months earlier than
 276 the CASSIOPPEE and PANDORA stations, reflecting the transit time of surface water flow
 277 from the Vitiaz Strait to the equator. The [Nd] difference reflects temporal variability in the
 278 enrichment of Nd within equatorial surface. Nevertheless, the enrichment in dissolved Nd at
 279 station GeoB17016, downstream of the river, of 1.3 pmol/kg still indicates an additional
 280 significant source. Even if we would assume an open ocean surface water [Nd] of 3.5
 281 pmol/kg (station GeoB17019, Fig. 3c) at Vitiaz Strait, and water transport as low as 0.5 Sv
 282 inside Vitiaz Strait to account for the fact that surface water at the equator during
 283 CASSIOPPEE was in Vitiaz Strait months earlier, the dissolved river input would only account
 284 for an additional 7% input of Nd to the flux of 8.0 t(Nd)/yr through Vitiaz Strait. This finding
 285 indicates that there is a significant source of REE input from PNG in addition to the river
 286 input. In the following, we discuss potential sources such as sediments and volcanic rocks
 287 from PNG, Sepik river particles, submarine groundwater discharge (SGD), benthic flux from
 288 pore waters, volcanic ash deposition, or admixture of northern hemisphere derived surface
 289 water.

290 Surface water derived from the northern hemisphere (e.g., station GeoB17014, ~6°N, 5-22 m
 291 water depth: ([Nd] = 4.5 ± 0.3 pmol/kg, $n = 2$, Fig. S3a) has lower dissolved [Nd] than that of
 292 our equatorial stations, and is thus not a potential source.

293 It has been shown that volcanic dust input from active volcanoes is a REE source in this
 294 region (e.g., Grenier et al., 2013; Pham et al., 2019). If volcanic dust input through ash
 295 deposition and dissolution would play a significant role in surface water REE enrichments of
 296 the zonal current system, we would also expect to find this enrichment signal in surface water
 297 flowing within the westward SEC. Yet, in contrast to the enriched equatorial eastward SC,
 298 surface water [REE] in the zonal westward SEC (stations 14, 19, 54, 57, 66) are similar to
 299 open ocean concentrations indicating lateral transport of preformed [REE] ($Nd_{norm} \sim 1$, Figs.

300 4a, b; 5a, b). This excludes the possibility of volcanic dust dissolution in the zonal current
 301 system as source for the elevated [REE]. In addition, low (Yb/Er)_N ratios of 0.55-0.69 in
 302 surface water within the SEC (Behrens et al., 2018a; this study) suggest preferential removal
 303 of the heaviest REEs from seawater along the transport path (Figs. 3b, 6a, b), likely due to
 304 adsorption of the heaviest REEs onto bacteria cell walls (e.g., Takahashi et al., 2005) and/or
 305 biogenic silica uptake (e.g., Akagi, 2013; Grenier et al., 2018). In contrast, surface water
 306 within the SC show slightly higher (Yb/Er)_N ratios of 0.79-0.84 suggesting recent input from
 307 PNG (Fig. 6b, c).

308 Moreover, our seawater-normalized REE patterns within the eastward SC are marked by an
 309 MREE enrichment (Fig. 5). This MREE enrichment is also observed for Sepik River water
 310 and sediment (Sholkovitz et al., 1999), PNG sediments and volcanic rocks (Grenier et al.,
 311 2013). In addition, several studies (e.g., Abbott et al., 2015; Johannesson et al., 2017) pointed
 312 out the importance of benthic REE flux from pore waters and SGD in the Pacific, and found
 313 MREE-enriched pore waters (e.g., Haley et al., 2004; Abbott et al., 2019) and SGD (Kim and
 314 Kim, 2011, 2014). However, to our knowledge, there is no SGD and pore water REE data
 315 reported from PNG. Here, we cannot differentiate between these particulate sources nor SGD
 316 or pore water input from PNG. The importance of PNG margin sediments as major source of
 317 TE input has also previously been suggested in several other studies on REE and Fe (Grenier
 318 et al., 2013; Labatut et al., 2014; Behrens et al., 2018a). Here we show for the first time, that
 319 the dissolved river input can only account for an additional 2-3.5% input of Nd to the annual
 320 flux of Nd through Vitiaz Strait, and that both fluxes cannot explain the REE enrichment in
 321 the eastward SC. This missing flux of 12.0-12.6 t(Nd)/yr originates from the PNG shelf.

322 At the transition of the zonal SEC and SC (stations 24 and 50), less enriched [REE] than in
 323 the SC (e.g., maximum Nd_{norm} of 1.28, Table S3) suggest mixing of SC and SEC source
 324 waters (Figs. 4a, b; 5 a, b). This is further supported by plots of salinity vs. [Nd] and [Yb], in

which the surface water data from stations 24 and 50 fall on a mixing line between high salinity, low [REE] extra-equatorial surface water of the SEC and low salinity, high [REE] equatorial water of the SC (Fig. 6a-c). This mixed surface water (together with the no enriched, preformed [REE] water of the zonal SEC) flows into the Solomon Sea via the Solomon Strait (Nd_{norm} up to 1.2, stations 60, 63) (Fig. 4a, b; 6a; Table S3).

Overall, our data indicate (1) elemental input largely from PNG margin sediments and transport via the NGCC to and within the equatorial eastward flowing SC, (2) westward lateral transport of preformed [REE] within the extra-equatorial SEC, and (3) lateral mixing of Eastern and Western Pacific source waters in the transition between the eastward and westward currents (SC, SEC) at $\sim 3^{\circ}S$. Our findings provide clear evidence for a discrete origin of the REE-enriched SC in the Tropical Western Pacific (more than 2-fold enriched [REE], Nd_{norm} up to 2.3, $(Yb/Er)_N$ ratios up to 0.84) compared to no enriched waters flowing within the zonal westward SEC (preformed [REE], $Nd_{norm} \sim 1$, $(Yb/Er)_N$ ratios as low as 0.55) and mixing at the transition of both currents (stations 24 and 50, Nd_{norm} up to 1.2). Moreover, our results are in line with the surface water distribution of total dissolvable [Fe] in our study area, that show highest values within the NGCC near the PNG margin ([Fe] up to 17 nM) and within the equatorial zonal eastward SC ([Fe] up to 0.9 nM) (Slemons et al., 2010, 2012) relative to those of the Coral and Solomon Seas that are fed by the westward SEC ([Fe] = 0.05-0.07 nM) (Obata et al., 2008) (Fig. 3e).

5.1.2. Near-surface water (40-100 m water depth)

Near-surface water normalization of [Nd] and [REE] to those of upstream station GeoB17019 (Behrens et al., 2018a, black inverted triangle in Fig. 4c) indicates a slight enrichment of REEs in the SC ($Nd_{norm} = 1.2-1.4$) (Fig. 5c). In combination with an elevated positive $(Eu/Eu^*)_N$ of near-surface water at the open ocean transect $165^{\circ}E$ ($(Eu/Eu^*)_N = 1.21 \pm 0.02$,

station 29, Fig. 2c) and at nearby stations GeoB17015 to -17 ($(\text{Eu}/\text{Eu}^*)_{\text{N}}$ up to 1.23, Behrens
 et al., 2018a) compared to stations 14 and 19 in the westward SEC ($(\text{Eu}/\text{Eu}^*)_{\text{N}} = 1.14 \pm 0.02$,
 Fig. 2c), this indicates trace element input from PNG and eastward transport to the equator
 via NGCC feeding the equatorial eastward SC. However, this near-surface water enrichment
 of REEs in the SC is lower than that of the overlying surface water ($\text{Nd}_{\text{norm}} = 1.7\text{-}2.3$) (Figs.
 4a-c; 5a-c), indicating a vertical decrease in [REE] in the SC towards 40-100 m water depth
 (e.g., 50% for [Nd] at station 69, Fig. 3c, d). This rapid [REE] decline with depth within the
 SC that cannot be related to the local bathymetry (all stations are deeper than 1400 m), is also
 observed for total dissolvable [Fe] within the NGCC near the PNG margin, decreasing by
 43% from the surface to near-surface (Slemons et al., 2010, 2012) (Fig. 3e, f). Given this
 vertical decline in surface to near-surface [Fe] near the PNG margin, and seeing that PNG is
 the source of the surface and near-surface trace element input found within the SC, we
 suggest that input to the surface layer near PNG explains this rapid decline with depth in
 [REE] (and probably [Fe]) within the surface mixed layer. In the westward SEC, on the other
 hand, similar surface and near-surface water [REE] (Fig. 3c, d), and no enriched REE
 patterns ($\text{Nd}_{\text{norm}} \sim 1$) (Figs. 4c; 5c), indicate westward lateral transport of preformed surface
 and near-surface water [REE] within the extra-equatorial SEC (stations, 14, 19, 54, 57, 66),
 except for the inflow into the Solomon Strait (station 63). Here, the vertical increase in
 surface to near-surface water [REE] (by ~ 2.3 pmol/kg [Nd] towards 51 m water depth), with
 a REE enrichment over upstream water (SEC) ($\text{Nd}_{\text{normalized}} = 1.93$), points to local REE input
 from the New Britain and New Ireland shelves (Figs. 4a-c; 5a-c). This is supported by
 physical observations in the Solomon Strait. In the western part of the Solomon Strait at 51 m
 water depth (station 63), current velocities are almost zero (or slightly positive indicating
 outflow, Fig. S2) suggesting that during the station, with the strong tide, the near-surface
 water gets probably enriched from both shelves inside and outside of the Solomon Sea.

375

376 **5.2. Temporal and spatial variability in surface and near-surface water REE**

377 **distributions in the study area**

378 The CASSIOPEE cruise took place at the onset of the strongest El Niño event of the early
379 21st century (ONI of +1.5 to +1.8) and coincides with strong westerly wind events during the
380 cruise (Delpech et al., 2019). That is, trace element input from the Tropical Western Pacific
381 volcanic islands (Grenier et al., 2013; this study) is influenced by island weathering being
382 related to precipitation during the SW monsoon period and the entrainment of this signal to
383 equatorial surface water (e.g., Milliman, 1995; Sholkovitz et al., 1999, see section 5.1.1.), that
384 is expected to be influenced by these intraseasonal and interannual climate fluctuations, with
385 stronger eastward surface currents during an El Niño event.

386 In order to evaluate the temporal variability in surface water REE input in the eastward SC,
387 we compare the surface water [Nd] during a strong El Niño year (station 69, CASSIOPEE
388 cruise, July-Aug., 2015), with strong eastward surface currents near the equator, with that
389 from a weak El Niño year (stations EUC-Fe 25 and 26, ONI = +0.5, EUC-Fe cruise, Aug.-
390 Sept. 2006, Slemons et al., 2010, 2012; Grenier et al., 2013), with weaker eastward currents
391 (Fig. S3a-c). Surface water [Nd] at stations EUC-Fe 26, 25 ([Nd] = 6.6 pmol/kg, 6.1 pmol/kg)
392 and station 69 ([Nd] = 8.1 pmol/kg) vary in [Nd] by 1.5-2 pmol/kg (Fig. S3a). In contrast,
393 northern hemisphere derived surface water (station GeoB17014, [Nd] = 4.6 pmol/kg, Behrens
394 et al., 2018a) is marked by lower [Nd] similar to that in the Vitiaz Strait (station 77, [Nd] =
395 4.9 pmol/kg, Pham et al., 2019) (Fig. S3a). Thus, this difference in the [Nd] for the
396 CASSIOPEE and EUC-Fe cruises likely indicates temporal variability of input and transport
397 in the PNG source area and the equatorial region, likely related to changes in ENSO
398 conditions. However, we are aware that nearby station EUC-Fe 25 is not sampled at exactly

the same location as station 69 (separated by 1°S, 3.5°E), and that we thus also observe a strong spatial variability in REE distribution.

In the Solomon Sea and its Straits, surface and near-surface waters of this study and the previous study of Pham et al. (2019) indicate spatial variability in REE distributions with [Nd] ranging from 3.3 pmol/kg up to 8.2 pmol/kg due to varying local continental inputs such as from the volcanic island margins and active volcanoes of New Britain and New Ireland ([Nd] = 5.2-8.2 pmol/kg, $Nd_{norm} = 1.5-2.4$, stations 63, this study, St. 36, St. 53, St. 57, St. 60, Pham et al., 2019) (Figs. 3c, e; 4b, c). In contrast, surface and near-surface waters of the westward SEC at all our stations (stations 14, 19, 54, 57, 66) and published stations (St. 10, St. 13, St. 43, GeoB17018-19, Behrens et al., 2018a; Pham et al., 2019) lack a significant variability in REE distributions, indicating no input and thus lateral transport of invariant preformed [REE] from the East Pacific ([Nd] = 3.5 ± 0.2 pmol/kg, $n = 22$, $Nd_{norm} \sim 1$) (Fig. 3a, c, d; 4a-c).

6. Conclusions

Our study presents dissolved surface to near-surface water REE concentrations ([REE]) (0-100 m water depth) at 10 stations in the zonal current system of the Tropical Western Pacific and two stations in the Solomon Strait, one of the areas where water enters the Solomon Sea. More than 2-fold enriched surface water [REE] in the equatorial zonal eastward surface current (SC) compared to the zonal westward South Equatorial Current (SEC) indicate significant elemental input. Flux calculations from combined geochemical data and ADCP current velocities indicate that this surface water input is largely derived from the basaltic Papua New Guinea margin sediments and/or Sepik River particles. Dissolved Sepik River input only accounts for an additional 2-3.5% input of Nd to the annual flux of Nd through Vitiaz Strait, which cannot explain the REE enrichment in the eastward SC.

424 We find temporal and spatial variability of surface water Nd input and transport in the PNG
 425 source area and the equatorial region within the eastward SC, with up to 2 pmol/kg higher
 426 [Nd] at the onset of the strongest El Niño event of the early 21st century (this study, July-
 427 Aug., 2015) compared to a weak El Niño year (Aug.-Sept. 2006, EUC-Fe cruise).
 428 In the Solomon Sea and its Strait, spatial variability in surface and near-surface water [REE]
 429 (this study and Pham et al., 2019) is related to varying local coastal inputs, particularly near
 430 New Ireland and New Britain. In the westward SEC, on the other hand, the lack of REE input
 431 and significant variability in REE distribution of this study and published data indicates
 432 lateral transport of preformed seawater [REE] into the study area.
 433 Our findings provide clear evidence for a discrete origin of the REE-enriched SC in the
 434 Tropical Western Pacific (more than 2-fold enriched [REE], Nd_{norm} up to 2.3, $(Yb/Er)_N$ ratios
 435 up to 0.84) compared to no enriched waters flowing within the zonal westward SEC
 436 (preformed [REE], $Nd_{norm} \sim 1$, $(Yb/Er)_N$ ratios as low as 0.55) and mixing at the transition of
 437 both currents (stations 24 and 50, Nd_{norm} up to 1.2).

438

439 **7. Acknowledgements**

440 We thank the scientific party, captain and crew of R/V *L'Atalante* cruise CASSIOPEE. We
 441 further thank M. Schulz for her help in the lab. The CASSIOPEE cruise
 442 (<https://doi.org/10.17600/15001200>) was supported by the French national programme
 443 LEFE/INSU, within the project ZEBRE. Financial support for this study came from the
 444 Deutsche Forschungsgemeinschaft (DFG, German Research Foundation) – 396302194
 445 through grant BE6184/2-1 to M. Behrens, the Institute for Chemistry and Biology of the
 446 Marine Environment (ICBM) and the Max Planck Institute for Marine Microbiology,
 447 Bremen.

448

8. References

- Abbott A. N., Haley B., McManus J. and Reimers C. (2015) The sedimentary source of dissolved rare earth elements to the ocean. *Geochim. Cosmochim. Acta* **154**, 186-200.
- Akagi T. (2013) Rare earth element (REE)–silicic acid complexes in seawater to explain the incorporation of REEs in opal and the “leftover” REEs in surface water: New interpretation of dissolved REE distribution profiles. *Geochim. Cosmochim. Acta* **113**, 174-192.
- Alberty M., Sprintall J., MacKinnon J., Gernineaud C., Cravatte S. and Ganachaud A. (2019) Moored observations of transport in the Solomon Sea. *J. Geophys. Res. Oceans* **124**, 8166-8192.
- Behrens M. K., Muratli J., Pradoux C., Wu Y., Böning P., Brumsack H.-J., Goldstein S. L., Haley B., Jeandel C., Paffrath R., Pena L. D., Schnetger B. and Pahnke K. (2016) Rapid and precise analysis of rare earth elements in small volumes of seawater - Method and intercomparison. *Mar. Chem.* **186**, 110-120.
- Behrens M. K., Pahnke K., Paffrath R., Schnetger B. and Brumsack H.-J. (2018a). Rare earth element distributions in the West Pacific: trace element sources and conservative vs. non-conservative behavior. *Earth Planet. Sci. Lett.* **486**, 166-177.
- Behrens M. K., Pahnke K., Schnetger B. and Brumsack H.-J. (2018b) Sources and processes affecting the distribution of dissolved Nd isotopes and concentrations in the West Pacific. *Geochim. Cosmochim. Acta* **222**, 508-534.
- Bonjean F. and Lagerloef G.S.E. (2002) Diagnostic model and analysis of the surface currents in the tropical Pacific ocean. *J. Phys. Oceanogr.* **32**, 2938-2954.
- Byrne R. H. and Kim K.-H. (1990) Rare earth element scavenging in seawater. *Geochim. Cosmochim. Acta* **54**, 2645-2656.

473 Cravatte S., Ganachaud A., Duong Q.-P., Kessler W. S., Eldin G. and Dutrieux P. (2011)
 474 Observed circulation in the Solomon Sea from SADCP data. *Prog. Oceanogr.* **88**, 116-
 475 130.

476 de Baar H. J. W., Bruland K. W., Schijf J., van Heuven S. M. A. C. and Behrens M. K.
 477 (2018) Low Cerium among the dissolved rare earth elements in the central North Pacific
 478 Ocean. *Geochim. Cosmochim. Acta* **236**, 5-40.

479 Delcroix T., Radenac M. H., Cravatte S., Alory G., Gourdeau L., Léger F., Singh A. and
 480 Varillon D. (2014) Sea surface temperature and salinity seasonal changes in the western
 481 Solomon and Bismarck Seas. *J. Geophys. Res.* **119**, 2642-2657.

482 Delpech A., Cravatte S., Marin F., Morel Y., Gronchi E. and Kestenare E. (2019) Observed
 483 tracer fields structuration by mid-depth zonal jets in the tropical Pacific. *J. Phys.*
 484 *Oceanogr.*, accepted. DOI:10.1175/JPO-D-19-0132.1

485 Elderfield H. and Greaves M. J. (1982) The rare earth elements in seawater. *Nature* **296**, 214-
 486 219.

487 Fine R. A., Lukas R., Bingham F. M., Warner M. J. and Gammon R. H. (1994) The western
 488 equatorial Pacific - a water mass crossroads. *J. Geophys. Res. Oceans* **99**, 25063-25080.

489 Ganachaud A., Cravatte S., Sprintall J., Germineaud C., Albery M., Jeandel C., Eldin G.,
 490 Metzl N., Bonnet S., Benavides M., Heimbürger L.-E., Lefèvre J., Michael S., Resing J.,
 491 Quéroùé F., Sarthou G., Rodier M., Berthelot H., Baurand F., Grelet J., Hasegawa T.,
 492 Kessler W., Kilepak M., Lacan F., Privat E., Send U., Van Beek P., Souhaut M. and
 493 Sonke J. E. (2017) The Solomon Sea: its circulation, chemistry, geochemistry and
 494 biology explored during two oceanographic cruises. *Elem. Sci. Anth.* **5**(0), 33.

495 Goldstein S. J. and Jacobsen S. B. (1988). REE in the Great Whale River estuary, northwest
 496 Quebec. *Earth Planet. Sci. Lett.* **88**, 241–252.

497 Grenier M., Jeandel C., Lacan F., Vance D., Venchiarutti C., Cros A. and Cravatte S. (2013)

498 From the subtropics to the central equatorial Pacific Ocean: Neodymium isotopic
 499 composition and rare earth element concentration variations. *J. Geophys. Res. Oceans*
 500 **118**, 592-618.

501 Grenier M., Jeandel C. and Cravatte S. (2014) From the subtropics to the equator in the
 502 Southwest Pacific: Continental material fluxes quantified using neodymium data along
 503 modeled thermocline water pathways. *Geophys. Res. Oceans* **119**, 3948–3966.

504 Grenier M., Garcia-Solsona E., Lemaitre N., Trull T. W., Bouvier V., Nonnotte P., van Beek
 505 P., Souhaut M., Lacan F., Jeandel C. (2018) Differentiating Lithogenic Supplies, Water
 506 Mass Transport, and Biological Processes On and Off the Kerguelen Plateau Using Rare
 507 Earth Element Concentrations and Neodymium Isotopic Compositions. *Front. Mar. Sci.*,
 508 5:426.

509 Haley B. A., Klinkhammer G. P. and McManus J. (2004) Rare earth elements in pore waters
 510 of marine sediments. *Geochim. Cosmochim. Acta* **68**, 1265-1279.

511 Hristova H. G. and Kessler W. S. (2012) Surface circulation in the Solomon Sea derived from
 512 Lagrangian drifter observations. *J. Phys. Oceanogr.* **42**, 448-458.

513 Johannesson K. H., Palmore C. D., Fackrell J., Prouty N. G., Swarzenski P. W., Chevis D. A.,
 514 Telfeyan K., White C. D. and Burdige D. J. (2017). Rare earth element behavior during
 515 groundwater–seawater mixing along the Kona Coast of Hawaii. *Geochim. Cosmochim.*
 516 *Acta* **198**, 229–258.

517 Kim I. and Kim G. (2011) Large fluxes of rare earth elements through submarine
 518 groundwater discharge (SGD) from a volcanic island, Jeju, Korea. *Mar. Chem.* **127**, 12–
 519 19.

520 Kim I. and Kim G. (2014) Submarine groundwater discharge as a main source of rare earth
 521 elements in coastal waters. *Mar. Chem.* **160**, 11–17.

522 Labatut M., Lacan F., Pradoux C., Chmeleff J., Radic A., Murray J. W., Poitrasson F.,
 523 Johansen A. M. and Thil F. (2014) Iron sources and dissolved-particulate interactions in
 524 the seawater of the Western Equatorial Pacific, iron isotope perspectives. *Glob.*
 525 *Biogeochem. Cycles* **28**, 1044-1065.

526 Lacan F. and Jeandel C. (2001) Tracing Papua New Guinea imprint on the central equatorial
 527 Pacific Ocean using neodymium isotopic compositions and rare earth element patterns.
 528 *Earth Planet. Sci. Lett.* **186**, 497-512.

529 Lacan F. and Jeandel C. (2005) Neodymium isotopes as a new tool for quantifying exchange
 530 fluxes at the continent-ocean interface. *Earth Planet. Sci. Lett.* **232**, 245-257.

531 Lindstrom E., Lukas R., Fine R., Godfrey S., Meyers G., Tsuchiya M. (1987) The western
 532 equatorial Pacific Ocean circulation study. *Nature* **330**, 533-537.

533 Milliman J. D. (1995) Sediment discharge to the ocean from mountainous rivers: the New
 534 Guinea example. *Geo-Mar. Lett.* **15**, 127-133.

535 Molina-Kescher M., Hathorne E.C., Osborne A.H., Behrens M.K., Kölling M., Pahnke K.
 536 and Frank M. (2018) The Influence of Basaltic Islands on the Oceanic REE Distribution:
 537 A Case Study From the Tropical South Pacific. *Front. Mar. Sci.*, 5:50.

538 Obata H., Shitashima K., Isshiki K. and Nakayama E. (2008) Iron, Manganese and
 539 Aluminium in upper waters of the Western South Pacific Ocean and its adjacent seas. *J.*
 540 *Oceanogr.* **64**, 233-245.

541 Pham V. Q., Grenier M., Cravatte S., Michael S., Jacquet S., Belhadj M., Nachez Y.,
 542 Germaineaud C. and Jeandel C. (2019) Dissolved rare earth elements distribution in the
 543 Solomon Sea. *Chem. Geol.* **524**, 11-36.

544 Radenac M.-H., Léger F., Messié M., Dutrieux P., Menkes C. and Eldin G. (2016) Wind-
 545 driven changes of surface current, temperature, and chlorophyll observed by satellites
 546 north of New Guinea. *J. Geophys. Res. Oceans* **121**, 2231– 2252.

547 Radic A., Lacan F. and Murray J. W. (2011) Iron isotopes in the seawater of the equatorial
 548 Pacific Ocean: New constraints for the oceanic iron cycle. *Earth Planet. Sci. Lett.* **306**, 1-
 549 10.

550 Reverdin G., Frankignoul C., Kestenare E. and McPhaden M. J. (1994) Seasonal variability
 551 in the surface currents of the equatorial Pacific. *J. Geophys. Res.: Oceans* **99**, 20323-
 552 20344.

553 Rousseau T. C. C., Sonke J. E., Chmeleff J., Van Beek P., Souhaut M., Boaventura G.,
 554 Seyler P. and Jeandel C. (2015) Rapid neodymium release to marine waters from
 555 lithogenic sediments in the Amazon estuary. *Nat. Commun.* **6**, 7592.

556 Schlitzer R. (2016) *Ocean Data View*, <http://odv.awi.de>.

557 Sholkovitz E. R., Elderfield H., Szymczak R. and Casey K. (1999) Island weathering: river
 558 sources of rare earth elements to the Western Pacific Ocean. *Mar. Chem.* **68**, 39-57.

559 Slemons L.O., Murray J.W., Resing J., Paul B. and Dutrieux P. (2010) Western Pacific
 560 coastal sources of iron, manganese and aluminum to the equatorial undercurrent. *Global*
 561 *Biogeochem. Cycles* **24**, GB3024.

562 Slemons L., Paul B., Resing J. and Murray J. W. (2012) Particulate iron, aluminum, and
 563 manganese in the Pacific equatorial undercurrent and low latitude western boundary
 564 current sources. *Mar. Chem.* **142-144**, 54-67.

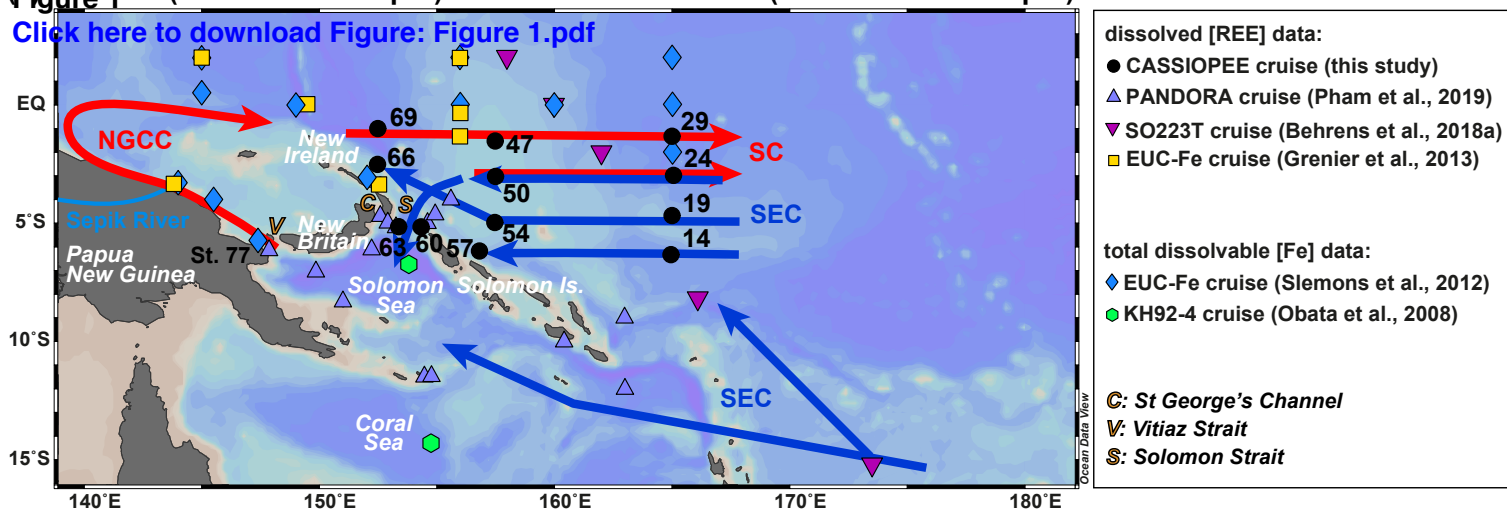
565 Takahashi Y., Chatellier X., Hattori K. H., Kato K. and Fortin D. (2005) Adsorption of rare
 566 earth elements onto bacterial cell walls and its implication for REE sorption onto natural
 567 microbial mats. *Chem. Geol.* **219**, 53-67.

568 Taylor S. R. and McLennan S. M. (1985) *The continental crust, its composition and*
 569 *evolution: An examination of the geochemical record preserved in sedimentary rocks.*
 570 Blackwell, Oxford.

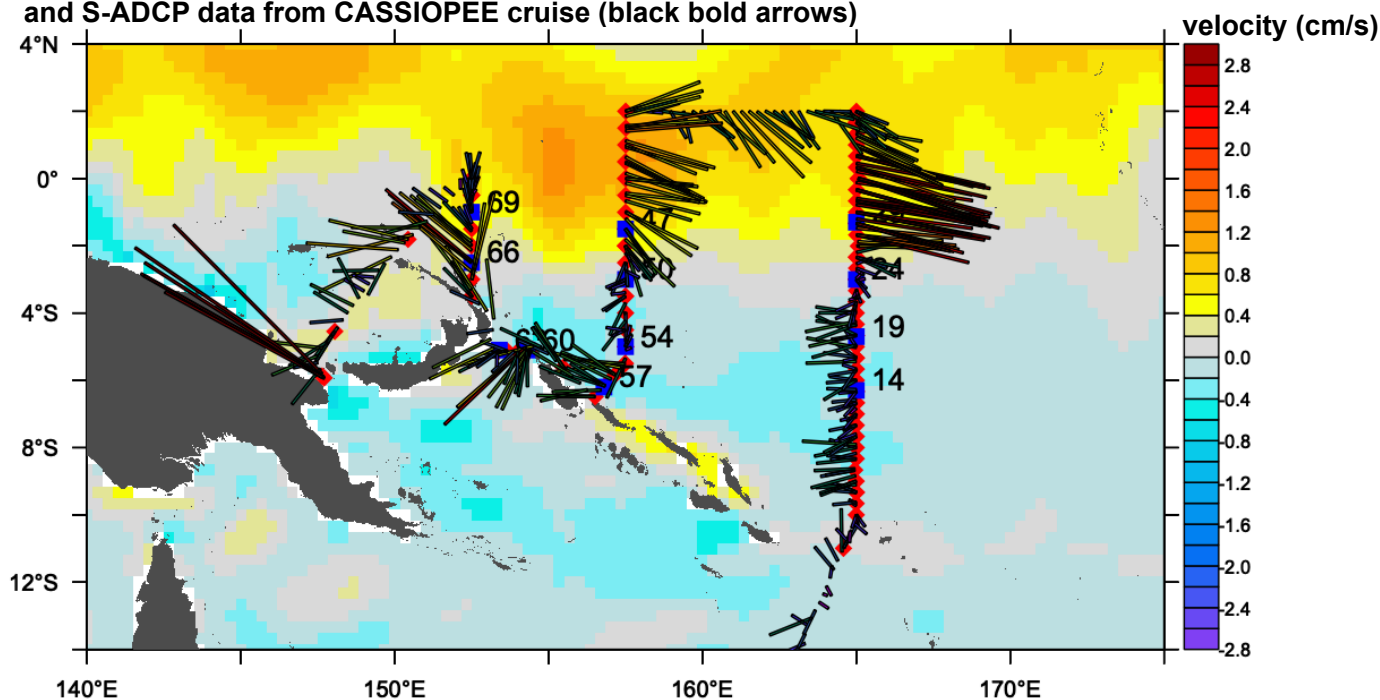
- 571 Woodhead J. D., Hergt J. M., Sandiford M. and Johnson W. (2010) The big crunch: physical
572 and chemical expressions of arc/continent collision in the western Bismarck Arc. *J.*
573 *Volcanol. Geotherm. Res.* **190**, 11-24.
- 574 Zhang Y., Lacan F. and Jeandel C. (2008) Dissolved rare earth elements tracing lithogenic
575 inputs over the Kerguelen Plateau (Southern Ocean). *Deep Sea Res. II* **55**, 638-652.

(a) Surface (0-35 m water depth) and near-surface water (40-100 m water depth)

[Click here to download Figure: Figure 1.pdf](#)

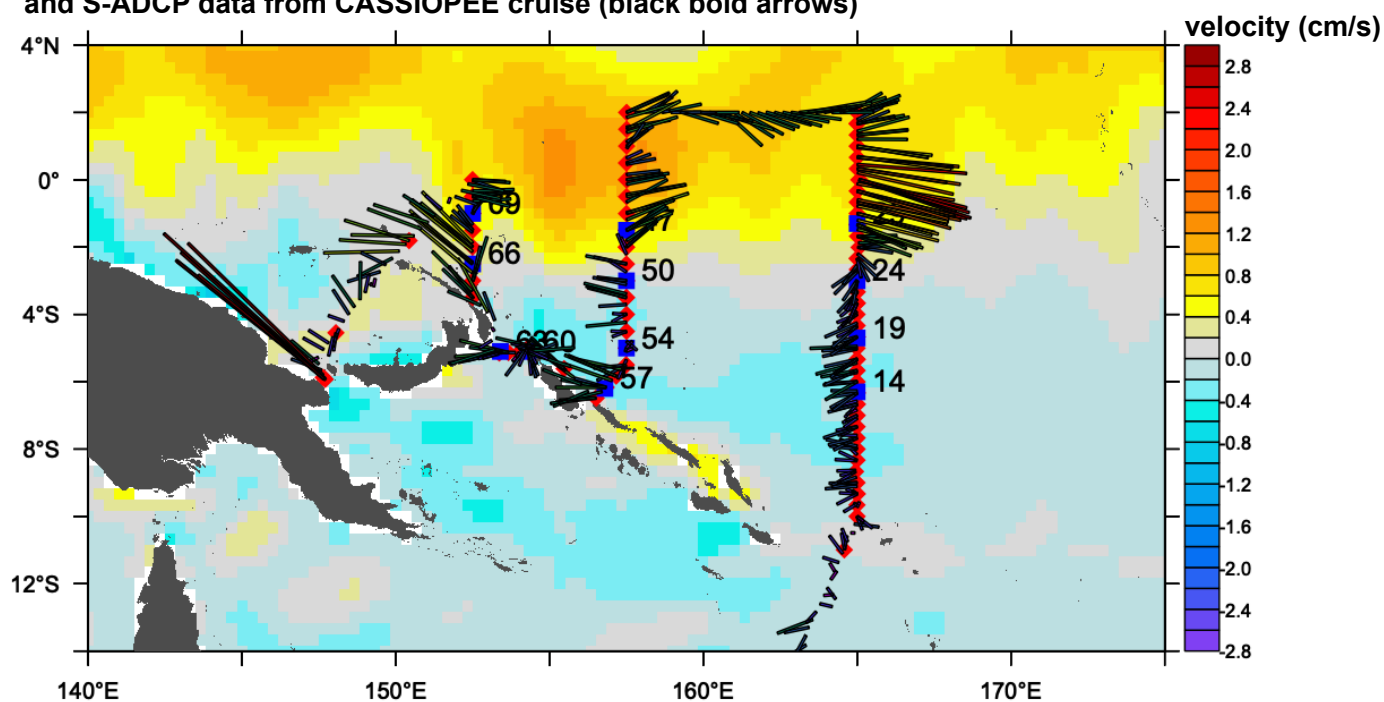


(b) Surface current velocities (10-35 m water depth) from OSCAR product (in color) in August 2015 and S-ADCP data from CASSIOPEE cruise (black bold arrows)

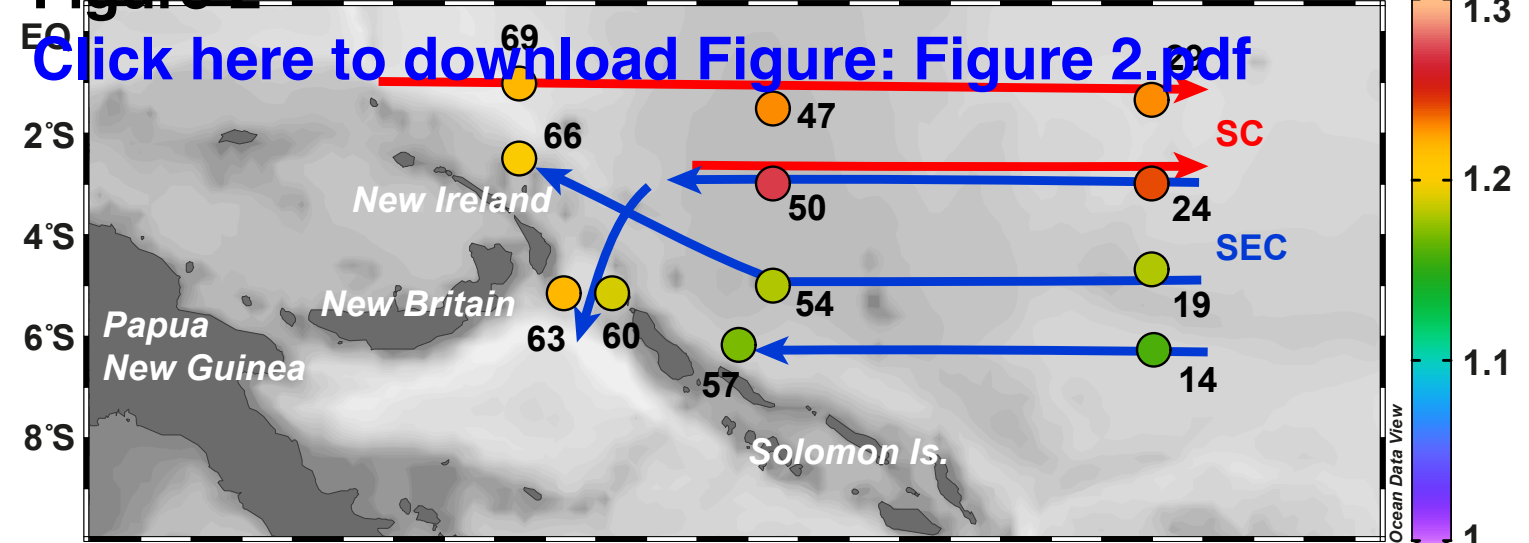


S-ADCP — 50 cm/s

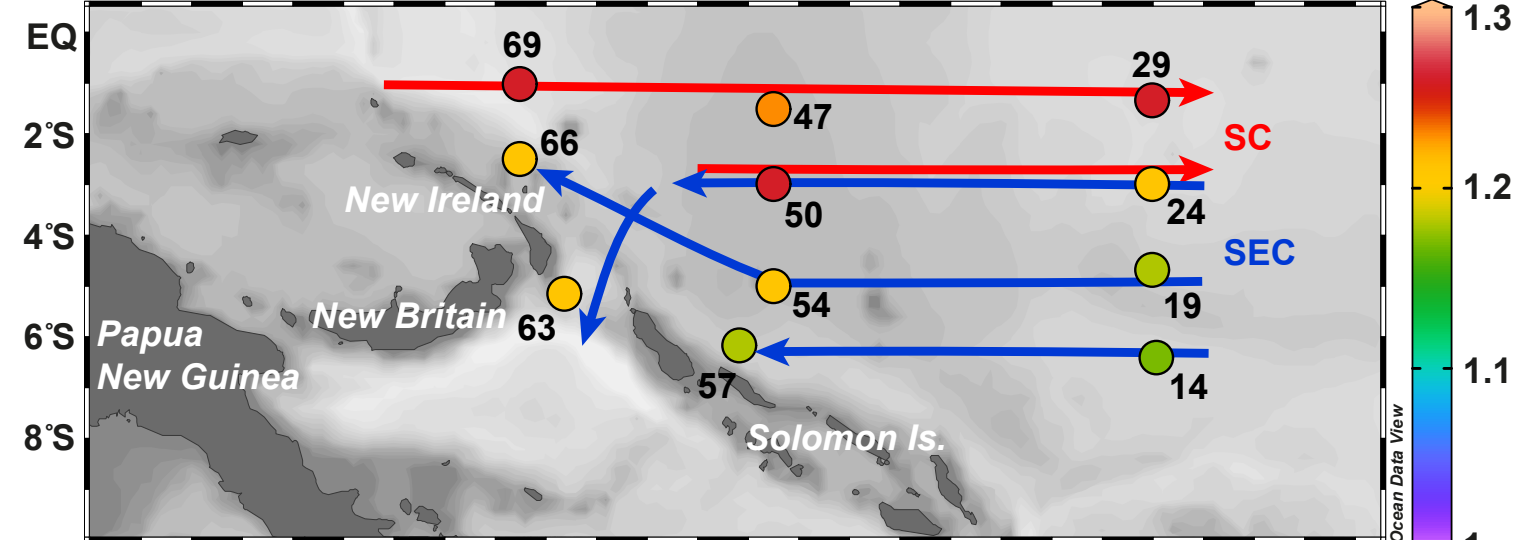
(c) Near-surface current velocities (40-100 m water depth) from OSCAR product (in color) in August 2015 and S-ADCP data from CASSIOPEE cruise (black bold arrows)



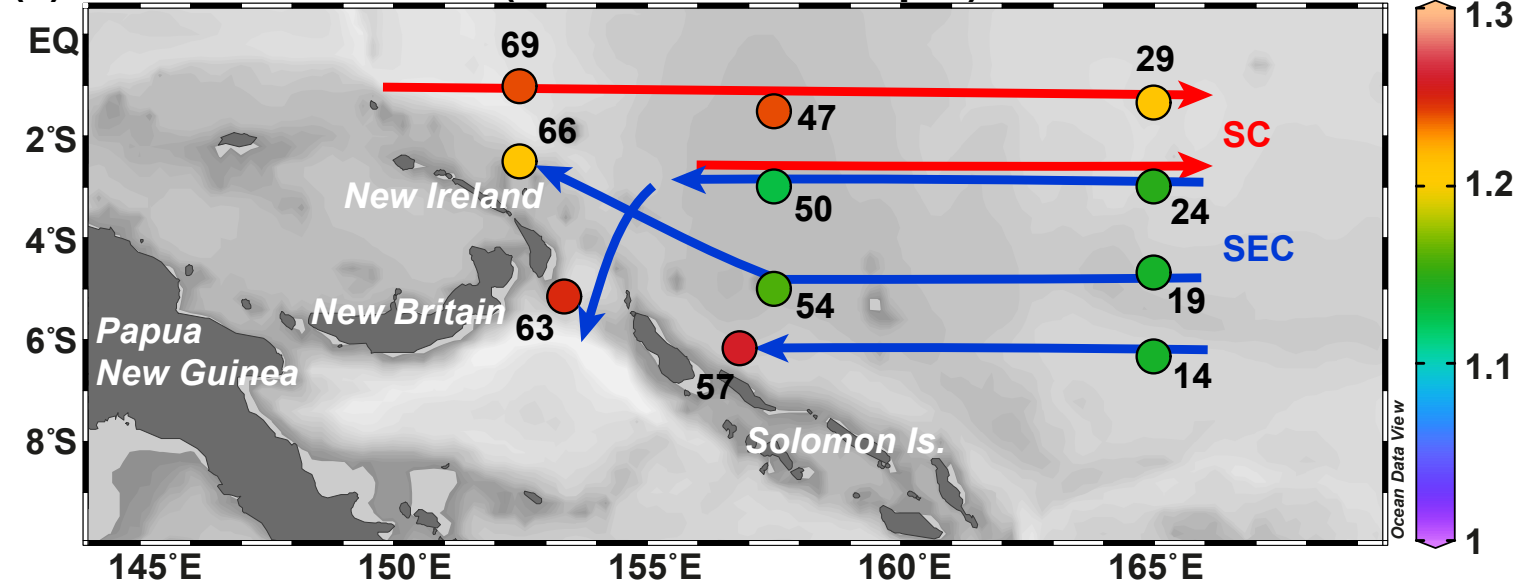
(a) Surface water (0-9 m water depth)

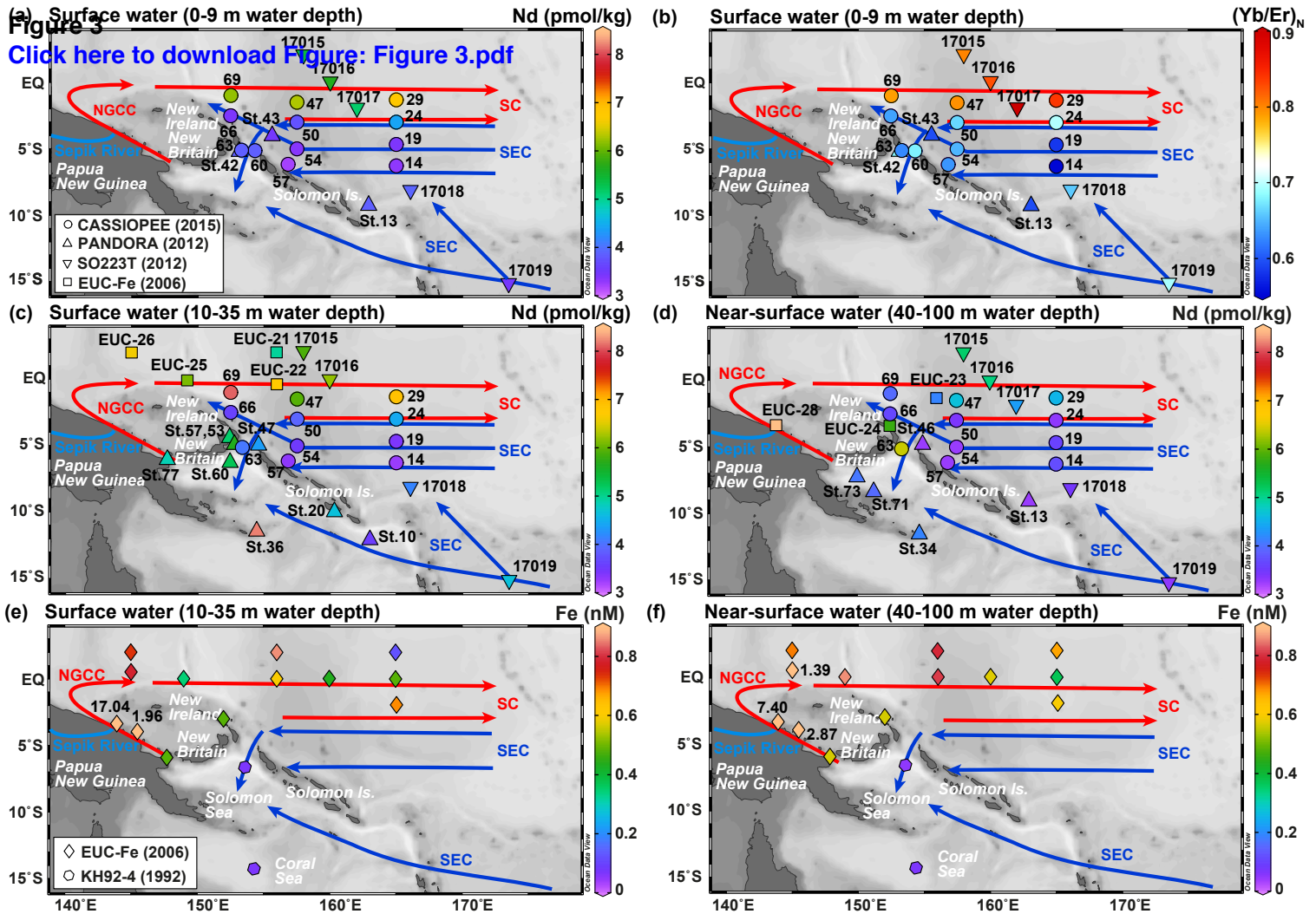


(b) Surface water (10-35 m water depth)



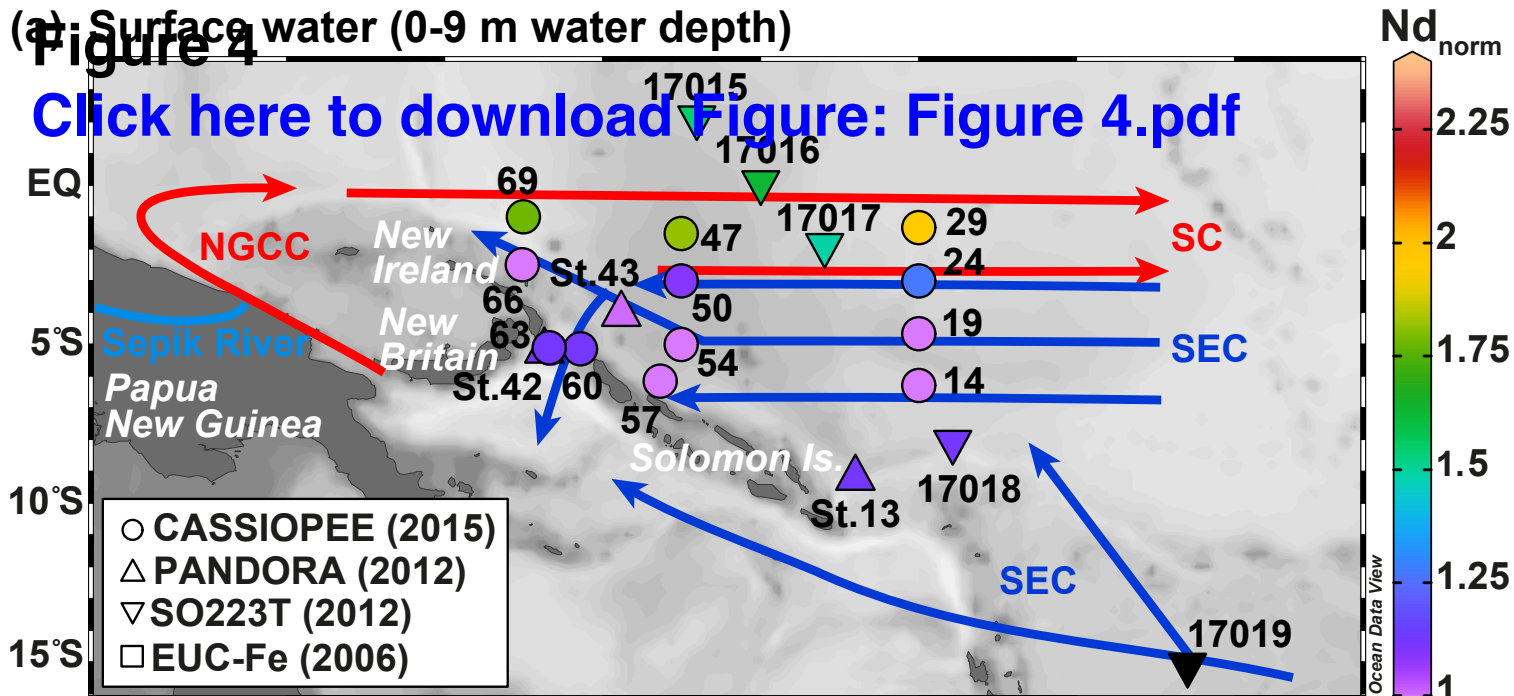
(c) Near-surface water (40-100 m water depth)



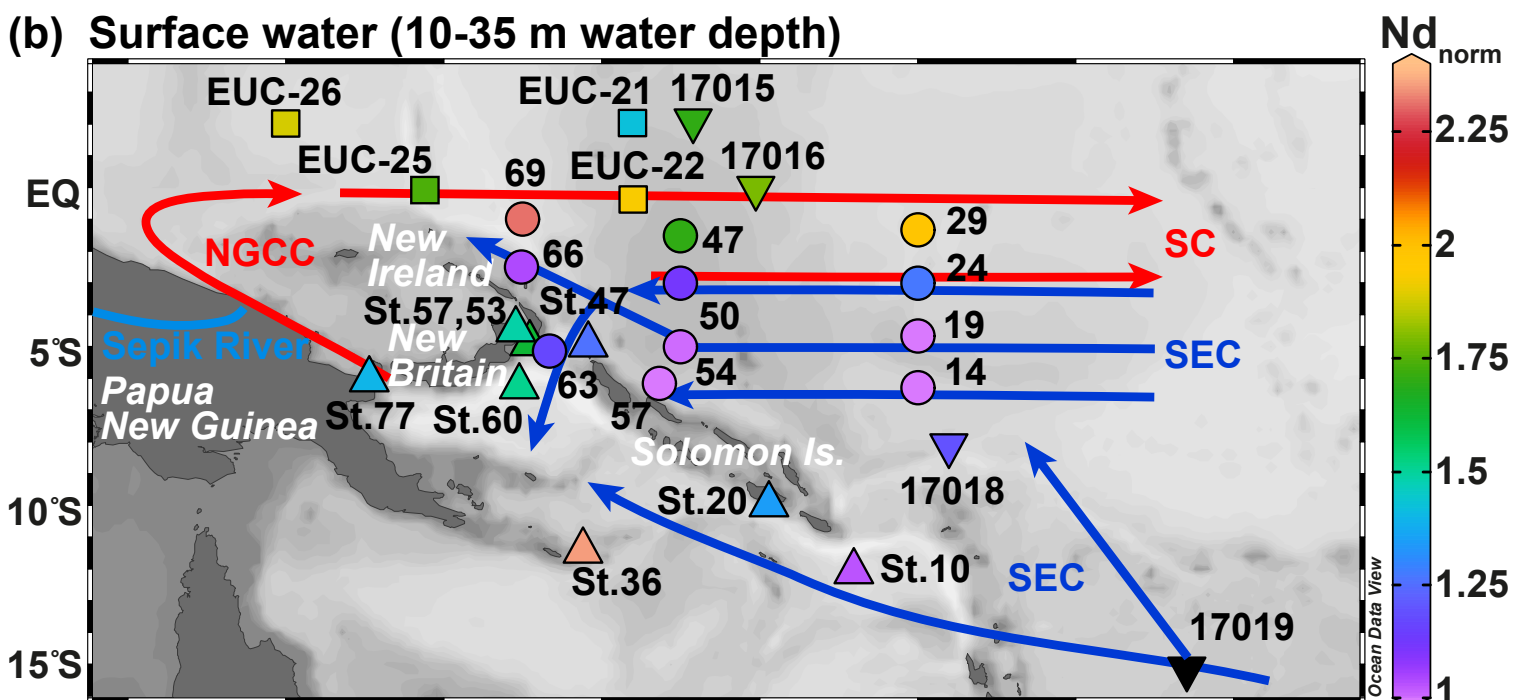


(a) Surface water (0-9 m water depth)

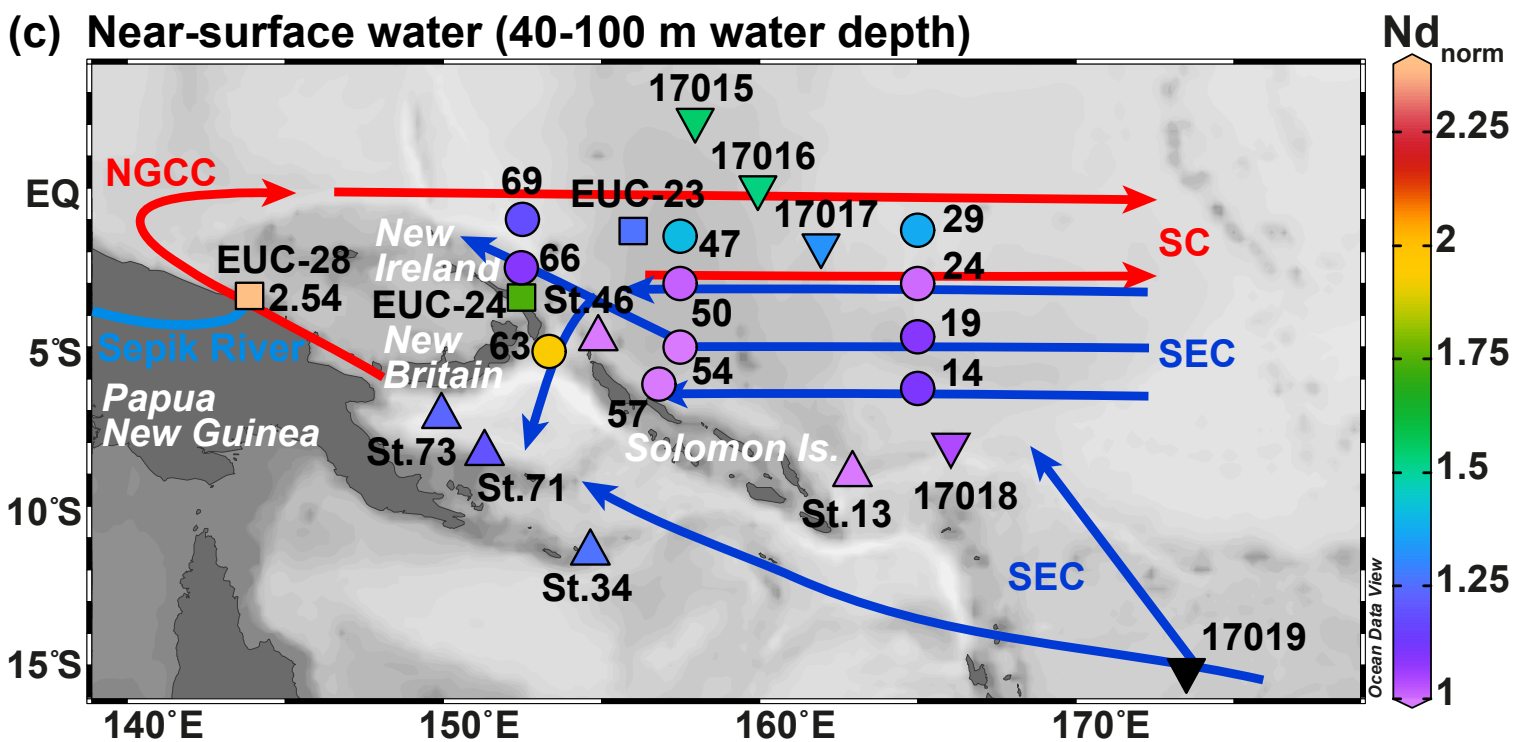
Click here to download Figure: Figure 4.pdf



(b) Surface water (10-35 m water depth)

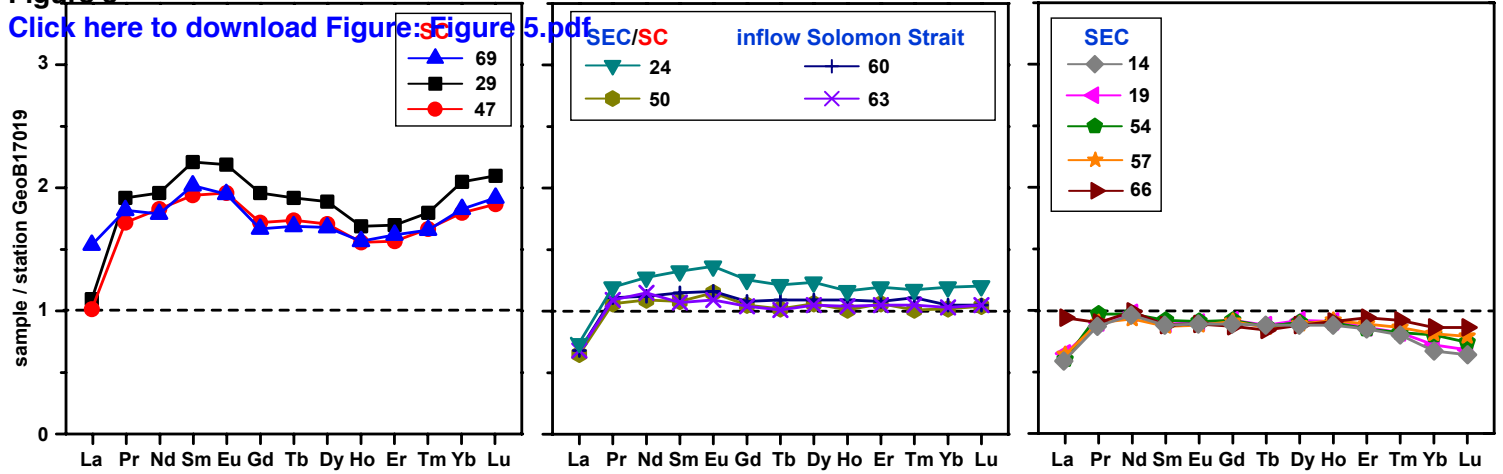


(c) Near-surface water (40-100 m water depth)

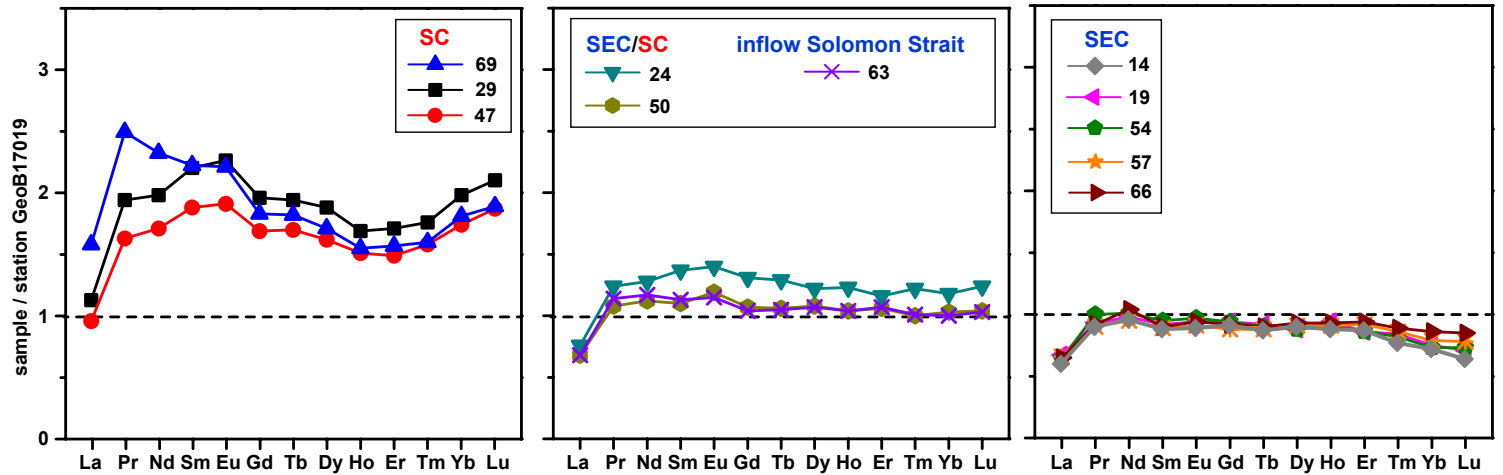


(a) Surface water (0-9 m water depth)

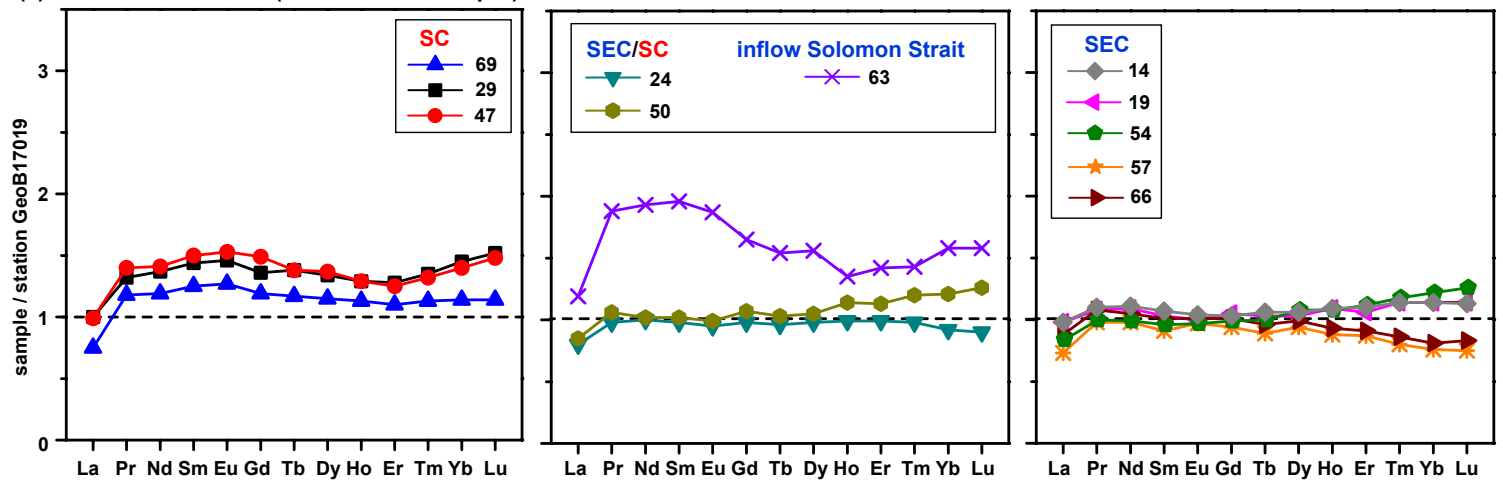
[Click here to download Figure: Figure 5.pdf](#)



(b) Surface water (10-35 m water depth)

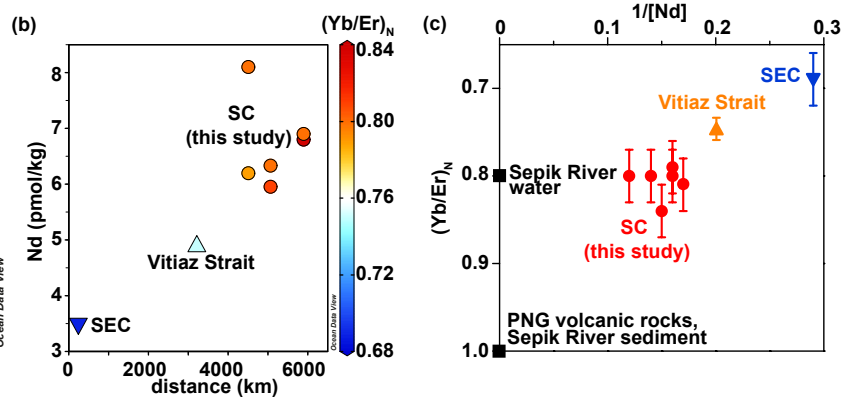
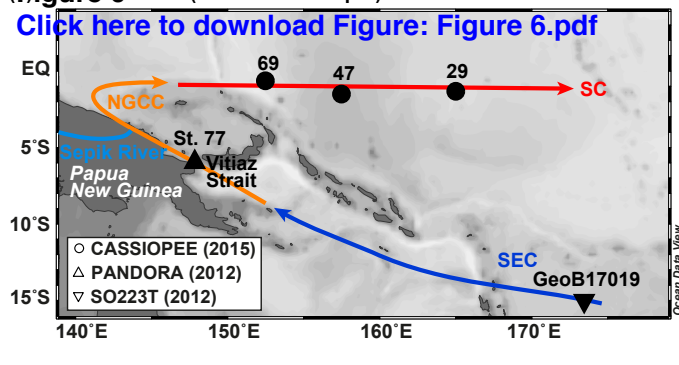


(c) Near-surface water (40-100 m water depth)



(Figure 6) surface water (0-35 m water depth)

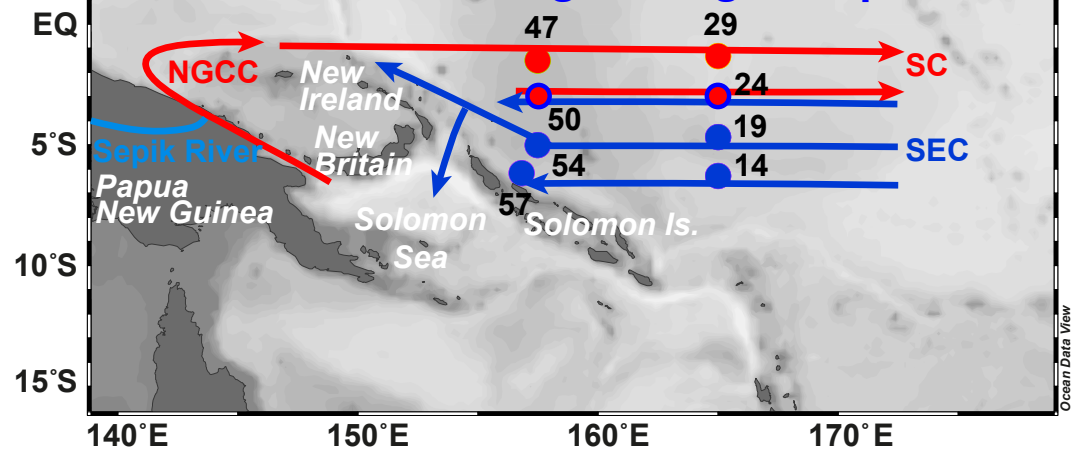
[Click here to download Figure: Figure 6.pdf](#)



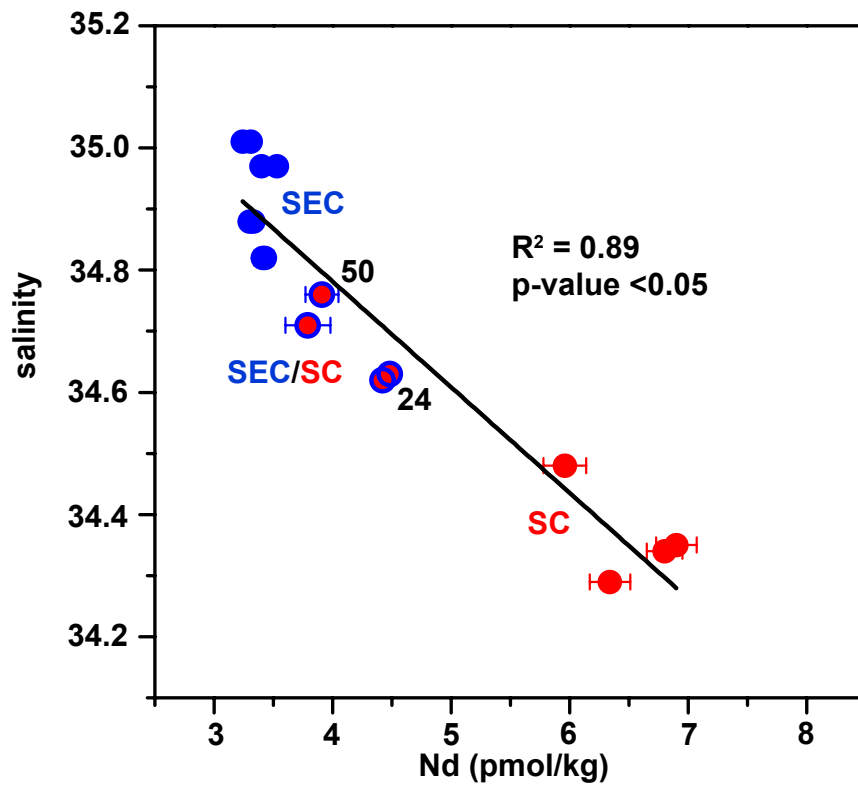
(a) Surface water (0-35 m water depth)

Figure 7

[Click here to download Figure: Figure 7.pdf](#)



(b)



(c)

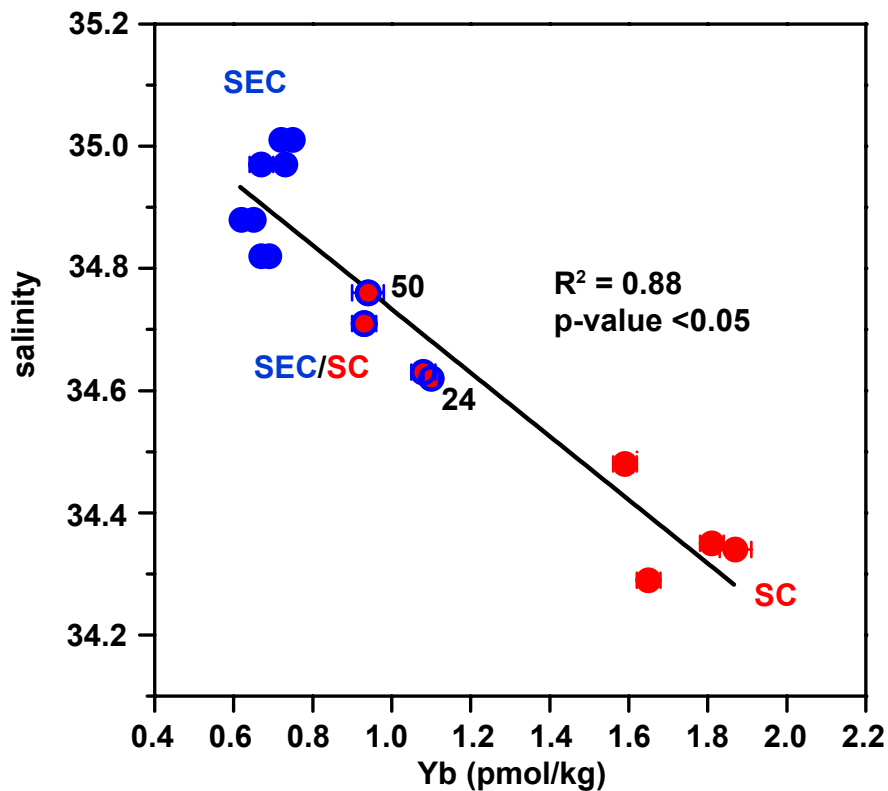


Figure captions

Fig. 1. (a) Map showing the station locations along the three meridional transects (152.5°E, 157.5°E, and 165°E) and in the Solomon Strait (stations 60, 63) (black dots, this study) of the CASSIOPEE cruise in the tropical West Pacific with eastward and westward currents, identified during the cruise using ADCP data are shown by red and blue arrows, respectively. Published stations mentioned in the text are marked by colored symbols (see legend) (Obata et al., 2008; Slemons et al., 2012; Grenier et al., 2013; Behrens et al., 2018a; Pham et al., 2019). Surface and near-surface currents: Surface Current (SC), South Equatorial Current (SEC), New Guinea Coastal Current (NGCC). This and all maps in following figures were created using Ocean Data View (Schlitzer, 2016). (b, c) Velocity of eastward and westward currents in red and blue colors, respectively, from OSCAR (<http://www.oscar.noaa.gov/>) product in August 2015 and superimposed in black bold arrows the S-ADCP currents from CASSIOPEE cruise (Delpech et al., 2019) at (b) 10-35 m water depth and (c) 40-100 m water depth. For reference to colors in this figure, the reader is referred to the web version of this article.

Fig. 2. Maps showing the distribution of PAAS-normalized (Taylor and McLennan, 1985) Eu anomalies $(Eu/Eu^*)_N$ for surface and near-surface waters of this study within westward (blue arrows) and eastward (red arrows) flowing currents (for abbreviations of currents see Fig. 1). For reference to colors in this figure, the reader is referred to the web version of this article.

Fig. 3. Maps showing the distribution of surface and near-surface water Nd concentrations (pmol/kg) (a, c, d) and PAAS-normalized (Taylor and McLennan, 1985) $(Yb/Er)_N$ ratios (b) from this study and published studies, and published total dissolvable Fe (nM) concentrations (e, f) (Obata et al., 2008; Slemons et al., 2012; station EUC-, Grenier et al., 2013; station 170-, Behrens et al., 2018a; station St., Pham et al., 2019) within the westward (blue arrows) and eastward (red arrows) flowing currents identified during the CASSIOPEE cruise using ADCP data. For abbreviations of currents see Fig. 1. For reference to colors in this figure, the reader is referred to the web version of this article.

Fig. 4. Maps showing the distribution of Nd concentrations normalized to those of upstream station GeoB17019 (Behrens et al., 2018a, black inverted triangle, normalized Nd concentrations referred to as Nd_{norm}) for all surface and near-surface water samples of this study and published stations (station EUC-, Grenier et al., 2013; station 170-, Behrens et al., 2018a; station St., Pham et al., 2019). For abbreviations of westward (blue) and eastward (red) flowing currents see Fig. 1. For reference to colors in this figure, the reader is referred to the web version of this article.

Fig. 5. REE concentrations normalized to those of upstream station GeoB17019 (Behrens et al., 2018a, black inverted triangle in Fig. 4a-c) for all surface and near-surface water samples of this study. For abbreviations of westward (blue) and eastward (red) flowing currents see Fig. 1. For reference to colors in this figure, the reader is referred to the web version of this article.

Fig. 6. (a) Map showing stations sampled for surface waters (0-35 m water depth) along a transect from the SEC (inverted triangle, Behrens et al., 2018a) via the Vitiaz Strait (triangle, Pham et al., 2019) to the SC (dot, this study) (for abbreviations of currents see Fig. 1), and (b) the transect distance (km), Nd concentrations and $(Yb/Er)_N$. (c) Plot of $(Yb/Er)_N$ vs. $1/[Nd]$ of surface waters along the transect with the distance in blue-red color scheme, along with $(Yb/Er)_N$ of PNG sources (black squares, volcanic rocks, Sepik River water and sediment, Sholkovitz et al., 1999; Woodhead et al., 2010). For abbreviations of currents see Fig. 1. For reference to colors in this figure, the reader is referred to the web version of this article.

Fig. 7. (a) Map showing stations sampled for surface waters (0-35 m water depth) within westward (blue dots and arrows) and eastward (red dots and arrows) flowing currents (for abbreviations of currents see Fig. 1), and (b, c) plots of salinity vs. Nd and Yb concentrations, showing a significant (p-value <0.05) correlation that indicates mixing of SC and SEC source waters at stations 24 and 50. For reference to colors in this figure, the reader is referred to the web version of this article.

Table 1
[Click here to download Table: Table 1.docx](#)

Table 1

Dissolved REE concentrations (pmol/kg) of seawater samples of this study.

Sample ID	Water depth (m)	La	Ce	Pr	Nd	Sm	Eu	Gd	Tb	Dy	Ho	Er	Tm	Yb	Lu
Station 14 (6.3328°S, 165.0002°E)															
1-7+8	6.7	3.10	1.37	0.69	3.33	0.66	0.20	1.17	0.18	1.40	0.37	1.17	0.14	0.62	0.09
1-5+6	29	3.09	1.38	0.70	3.30	0.65	0.20	1.19	0.18	1.42	0.36	1.19	0.13	0.65	0.09
1-3+4	94	3.92	1.53	0.80	3.72	0.74	0.23	1.27	0.21	1.63	0.46	1.54	0.20	1.07	0.16
Station 19 (4.6660°S, 164.9987°E)															
1-7+8	6	3.37	1.49	0.71	3.43	0.67	0.21	1.22	0.18	1.46	0.38	1.19	0.14	0.67	0.10
1-5+6	26	3.49	1.52	0.73	3.41	0.69	0.21	1.24	0.19	1.40	0.39	1.19	0.15	0.69	0.10
1-3+4	60	3.91	1.96	0.79	3.63	0.72	0.22	1.29	0.20	1.58	0.46	1.49	0.20	1.06	0.17
Station 24 (3.0007°S, 165.0022°E)															
1-7+8	6	3.84	2.38	0.94	4.42	0.99	0.31	1.65	0.25	1.96	0.49	1.64	0.20	1.10	0.17
1-5+6	26	3.96	2.31	0.98	4.48	1.02	0.32	1.73	0.26	1.94	0.52	1.60	0.21	1.08	0.17
1-3+4	71	3.21	1.26	0.71	3.33	0.68	0.21	1.21	0.19	1.50	0.41	1.38	0.17	0.86	0.13
Station 29 (1.3338°S, 165.0032°E)															
1-7+8	9	5.67	4.12	1.51	6.80	1.65	0.50	2.58	0.40	3.00	0.70	2.33	0.30	1.87	0.29
1-5+6	25	5.90	4.20	1.53	6.90	1.64	0.51	2.59	0.40	3.00	0.71	2.37	0.30	1.81	0.29
1-3+4	89	4.01	2.40	0.96	4.56	1.00	0.32	1.68	0.27	2.05	0.54	1.79	0.24	1.36	0.22
Station 47 (1.4987°S, 157.5003°E)															
2-15+16	4.4	5.26	3.77	1.35	6.34	1.45	0.45	2.25	0.36	2.70	0.65	2.16	0.28	1.65	0.26
2-11+12	25	5.02	3.35	1.28	5.96	1.40	0.43	2.23	0.35	2.58	0.63	2.05	0.27	1.59	0.26
2-6+7	60	3.97	2.48	1.02	4.69	1.04	0.33	1.84	0.27	2.09	0.54	1.75	0.23	1.31	0.22
Station 50 (3.0012°S, 157.5003°E)															
1-7+8	4	3.38	1.92	0.84	3.79	0.81	0.26	1.38	0.21	1.69	0.43	1.46	0.17	0.93	0.15
1-5+6	24	3.56	1.76	0.85	3.91	0.82	0.27	1.41	0.22	1.72	0.44	1.47	0.17	0.94	0.15
1-3+4	55	3.40	1.44	0.77	3.42	0.71	0.22	1.32	0.20	1.61	0.48	1.58	0.21	1.13	0.18
Station 54 (4.9988°S, 157.4995°E)															
1-9+10	5	3.13	1.54	0.76	3.40	0.69	0.21	1.21	0.18	1.44	0.38	1.18	0.14	0.73	0.10
1-7+8	24	3.35	1.70	0.79	3.53	0.71	0.22	1.24	0.18	1.41	0.38	1.19	0.14	0.67	0.10
1-5+6	74	3.35	1.46	0.73	3.30	0.67	0.21	1.22	0.20	1.66	0.45	1.56	0.21	1.14	0.18
Station 57 (6.1663°S, 156.8328°E)															
1-7+8	6	3.32	1.33	0.71	3.24	0.66	0.20	1.21	0.18	1.42	0.39	1.23	0.15	0.75	0.11
1-5+6	10	3.45	1.30	0.71	3.31	0.66	0.21	1.16	0.18	1.44	0.38	1.27	0.15	0.72	0.11
1-3+4	45	2.94	1.37	0.71	3.26	0.64	0.21	1.16	0.18	1.44	0.37	1.22	0.14	0.71	0.11
Station 60 (5.1417°S, 154.3325°E)															
1-21+22	8	3.54	2.45	0.88	3.90	0.86	0.27	1.43	0.23	1.74	0.46	1.49	0.19	0.97	0.15
Station 63 (5.1378°S, 153.3665°E)															
1-7+8	6	3.55	2.30	0.86	4.01	0.80	0.25	1.37	0.21	1.66	0.44	1.45	0.18	0.94	0.15
1-5+6	26	3.55	2.53	0.90	4.07	0.84	0.26	1.37	0.21	1.71	0.44	1.48	0.17	0.91	0.14
1-3+4	51	4.77	5.9*	1.37	6.44	1.36	0.41	2.02	0.30	2.39	0.57	1.98	0.25	1.47	0.23
Station 66 (2.4983°S, 152.4945°E)															
1-17+18	4	4.92	1.99	0.71	3.45	0.66	0.20	1.15	0.18	1.41	0.38	1.29	0.16	0.79	0.12
1-15+16	10	3.26	1.35	0.73	3.82	0.66	0.21	1.24	0.18	1.46	0.39	1.26	0.15	0.77	0.12
1-9+10	25	3.49	1.76	0.73	3.46	0.69	0.21	1.18	0.18	1.51	0.39	1.33	0.15	0.79	0.12
1-7+8	51	3.54	1.80	0.79	3.49	0.70	0.22	1.24	0.19	1.52	0.39	1.27	0.15	0.76	0.12
1-1+2	100	4.88	2.49	0.88	3.83	0.77	0.25	1.35	0.21	1.74	0.49	1.62	0.22	1.24	0.21
Station 69 (0.9993°S, 152.5010°E)															
1-7+8	6	8.01	4.32	1.43	6.20	1.51	0.45	2.19	0.35	2.66	0.65	2.22	0.28	1.68	0.27
1-5+6	25	8.27	10*	1.96	8.10	1.66	0.50	2.42	0.37	2.73	0.65	2.16	0.28	1.65	0.26
1-3+4	56	3.00	2.05	0.86	3.96	0.87	0.28	1.47	0.23	1.75	0.47	1.54	0.20	1.07	0.17

*questionable data.